PUBLICATIONS OF
THE UNIVERSITY OF EASTERN FINLAND

Dissertations in Forestry and Natural Sciences

SATU INKINEN

ULTRASOUND BACKSCATTERING IN ARTICULAR CARTILAGE

Experimental and finite difference time domain simulation studies of ultrasound backscatter arising from chondrocytes and collagen

UNIVERSITY OF
EASTERN FINLAND

PUBLICATIONS OF THE UNIVERSITY OF EASTERN FINLAND
DISSERTATIONS IN FORESTRY AND NATURAL SCIENCES

N:o 265

Satu Inkinen

ULTRASOUND BACKSCATTERING IN ARTICULAR CARTILAGE

EXPERIMENTAL AND FINITE DIFFERENCE TIME DOMAIN SIMULATION STUDIES OF ULTRASOUND BACKSCATTER ARISING FROM CHONDROCYTES AND COLLAGEN

ACADEMIC DISSERTATION

To be presented by the permission of the Faculty of Science and Forestry for public examination in the Auditorium MS301 in Medistudia Building at the University of Eastern Finland, Kuopio, on April 21th, 2017, at 12 o'clock.

University of Eastern Finland
Department of Applied physics
Kuopio 2017

Grano Oy
Jyväskylä, 2017
Editors: Pertti Pasanen, Pekka Toivanen,
Jukka Tuomela, and Matti Vornanen

Distribution:
University of Eastern Finland Library / Sales of publications
julkaisumyynti@uef.fi
http://www.uef.fi/kirjasto

ISBN: 978-952-61-2467-4 (print)
ISSNL: 1798-5668
ISSN: 1798-5668
ISBN: 978-952-61-2468-1 (pdf)
ISSNL: 1798-5668
ISSN: 1798-5676 (pdf)

Author's address:
University of Eastern Finland
Department of Applied Physics
P.O.Box 1627
70211 KUOPIO
FINLAND
email: satu.inkinen@uef.fi

Supervisors:
Professor Juha Töyräs
University of Eastern Finland
Department of Applied Physics
P.O.Box 1627
70211 KUOPIO
FINLAND
email: juha.toyras@uef.fi

Adjunct Professor Tuomas Virén
University of Eastern Finland
Department of Applied Physics
P.O.Box 1627
70211 KUOPIO
FINLAND
email: tuomas.viren@kuh.fi

Reviewers:
Professor, Yong Ping Zheng
The Hong Kong Polytechnic University
Interdisciplinary Division of Biomedical Engineering
Hong Kong , China
email: yongping.zheng@polyu.edu.hk

Professor Quentin Grimal
Sorbonne Universités, UPMC
Laboratoire d'Imagerie Biomédicale
Paris, France
email: quentin.grimal@upmc.fr

Opponent:
Assistant Clinical Professor Jonathan J. Kaufman
The Mount Sinai School of Medicine
Department of Orthopaedics
New York, NY, USA
email: jjkaufman@cyberlogic.org

Satu Inkinen
Ultrasound backscattering in articular cartilage Experimental and finite difference time domain simulation studies of ultrasound backscatter arising from chondrocytes and collagen
Kuopio: University of Eastern Finland, 2017
Publications of the University of Eastern Finland
Dissertations in Forestry and Natural Sciences

ABSTRACT

Quantitative ultrasound techniques have been developed for investigating healthy, osteoarthritic (OA) and repaired articular cartilage. During arthroscopy, ultrasound imaging has been used in the evaluation of the early signs of OA as well as in the detection and grading of cartilage injuries. Ultrasound techniques can be applied not only for evaluation of the cartilage surface but also for assessing subsurface properties by analysing the backscatter signal. However, there is still no complete understanding of how different cartilage components, such as collagen network and chondrocytes, influence ultrasound backscatter.

The aim of this thesis was to investigate both experimentally and computationally how collagen and chondrocytes affect ultrasound backscatter. In study **I**, agarose gel constructs with varying collagen or chondrocyte concentrations were prepared and the backscatter intensity was measured using 9 and 40 MHz ultrasound transducers suited for ultrasound arthroscopy. In study **II**, the anisotropy of ultrasound backscatter was determined experimentally. In study **III**, the finite difference time domain (FDTD) simulations of ultrasound scattering in agarose gel constructs with varying concentrations of collagen or chondrocytes were constructed to mimic the experimental setup used in study **I**. In study **IV**, the effect of chondrocytes in superficial cartilage on ultrasound backscatter was investigated numerically and experimentally. In order to obtain material parameters of chondrocytes and the extracellular matrix for the FDTD simulations, fixed cartilage sections were scanned in a 250-MHz scanning acoustic microscope (SAM). Furthermore, human cartilage samples were scanned using 50-MHz SAM to investigate the dependency of coherent scattering and cell spacing experimentally *ex vivo*.

Ultrasound backscattering differed significantly ($p < 0.05$) between scaffolds with different concentrations of collagen and chondrocytes (study **I**). Ultrasound backscatter was found to be anisotropic in cartilage and when ultrasound imaging was conducted in a direction perpendicular to the orientation of collagen fibers, the scattering intensity was highest (study **II**). The results of FDTD simulations in study **III** correlated with the experimental results in study **I** and a similar increase in the ultrasound backscatter was observed as a function of collagen or chondrocyte concentration. In study **IV**, FDTD simulations with layered cell structures displayed a peak in the depth dependent frequency spectrum due to coherent scattering. The cell spacing could be estimated from that peak and an excellent correlation ($R^2 = 0.99$, $p < 0.05$) was found between the estimated and simulated spacing with an average error of 0.2 µm. In study **IV**, the mean cell spacing estimated from 50-MHz SAM was 28.3 ± 5.3 µm. A strong correlation ($R^2 = 0.59$, $p \leq 0.001$) between spacing estimates from light microscopy (LM) and 50-MHz SAM was found for samples with Mankin score ≤ 3. Moreover, significant correlations between LM spacing estimates

and conventional ultrasound backscatter parameters (*AFB* and *AIB*) were found for Mankin score ≤ 3 samples (*AFB*: $R^2 = 0.64$, $p < 0.0001$, *AIB*: $R^2 = 0.79$, $p < 0.0001$).

To conclude, the present results indicate that ultrasound backscatter measured from articular cartilage is sensitive to changes in the composition and structure of the collagen network and the number and distribution of chondrocytes. However, further research will be needed to optimize backscatter analysis techniques in the characterization of articular cartilage. These backscatter techniques could be applied in different procedures, for example when monitoring the growth of articular cartilage constructs in a bioreactor and during the arthroscopic evaluation of articular cartilage and other connective tissues in a joint.

National Library of Medicine Classification: *QT 34, QT 36, WE 300, WN 180, WN 208*
Medical Subject Headings: *Diagnostic Imaging/methods; Ultrasonics; Ultrasonography; Ultrasonic Waves; Cartilage, Articular; Chondrocytes; Collagen; Extracellular Matrix; Extracellular Space; Anisotropy; Numerical Analysis, Computer-Assisted; Computer Simulation*
Yleinen suomalainen asiasanasto: *kuvantaminen; ultraääni; ultraäänitutkimus; rusto; nivelrusto; kollageenit; soluväliaine; numeerinen analyysi; simulointi*

ACKNOWLEDGEMENTS

This study was carried out in the Department of Applied Physics at the University of Eastern Finland and Kuopio University Hospital during years 2013–2017.

First, I would like to thank my supervisors Professor Juha Töyräs Ph.D. and Adjunct Professor Tuomas Virén Ph.D. for their guidance throughout the thesis work. I'm deeply grateful to Juha, whose enthusiasm on science and research and hard work mentality have truly inspired me on my research journey. I want to thank Tuomas especially during the beginning of my thesis for his help in the lab and for his readiness to help whenever need be.

I would like to express my deepest gratitude to all co-authors. These studies could not have been completed without your contribution.

I want to thank the official reviewers of this thesis, Professor Yong Ping Zheng Ph.D. and Professor Quentin Grimal Ph.D., for their professional comments and constructive criticism. I also want to thank Ewen MacDonald, D.Pharm., for linguistic review.

I would like to express my deepest graditude to the Dean Jukka Jurvelin Ph.D. for giving me the opportunity to join the Biophysics of Bone and Cartilage (BBC) research group as summer worker. Since the summer of 2011, I have been privileged to work with many intelligent, supportive and helpful colleagues within the BBC-group.

I want to thank my colleagues, especially my 'ex-roommates' Jukka Liukkonen and Pia Puhakka for many helpful discussions in the office and Markus Malo for his help and support in daily problems. I also want to thank namely the emeritus members Jari Rautiainen, Juuso Honkanen, Kimmo Halonen, Chibuzor Eneh and the current members namely Weiwei, Mikko, Kata, Anni, Jaakko, Simo, Mimmi, Ari, Abhisek, Jari, Mithu, Miitu, Gustavo, Aapo, Niina and all the rest of the BBC group. Thank you. It has been a great time.

I'm deeply grateful for my friends outside the academic world for your support outside the office hours. Especially, I want to thank Riina Repo, Tuomas Paulin, Minna Rozendaal, Jenna Veera Asikainen, Laura Känninen, Riikka Pieviläinen and Anna-Mari Kilpijärvi. I wish to give special thanks to Marko Häkkinen for giving me the chance to tag along to the fly fishing and hiking trips whenever I had the chance to take my mind off the thesis.

Finally, I want to thank my parents Seija and Antti Inkinen for your support and encouragement throughout the years.

The financial support from Kuopio University Hospital, Academy of Finland, and the Doctoral Programme in Science, Technology and Computing (SCITECO) is acknowledged.

Kuopio, March 15, 2017

Satu Inkinen

LIST OF PUBLICATIONS

This thesis consists of a review of the author's work in the field of ultrasound imaging of articular cartilage and the following selection of the author's publications:

I Inkinen S., Liukkonen J., Ylärinne J.H., Puhakka P.H., Lammi M.J., Virén T., Jurvelin J.S., Töyräs J., "Collagen and chondrocyte concentrations control ultrasound scattering in agarose scaffolds," *Ultrasound in Medicine and Biology*. **40**, 2162–71, (2014).

II Inkinen S.I., Liukkonen J., Tiitu V., Virén T., Jurvelin J.S., Töyräs J., "Ultrasound backscattering is anisotropic in bovine articular cartilage," *Ultrasound in Medicine and Biology*. **41**, 1958–66, (2015).

III Inkinen S.I., Liukkonen J., Malo M. K.H., Virén T., Jurvelin J.S., Töyräs J., "Finite difference time domain model of ultrasound propagation in agarose scaffold containing collagen or chondrocytes," *The Journal of the Acoustical Society of America*, **141**, 1–7, (2016).

IV Rohrbach D., Inkinen S.I., Zatloukalová J., Kadow-Romacker A., Joukainen A., Malo M., Mamou J., Töyräs J., Raum K., "Regular chondrocyte spacing is a potential cause for coherent ultrasound backscatter in human articular cartilage," *Accepted for publication*, (2017).

Throughout the overview, these papers will be referred to by Roman numerals.

AUTHOR'S CONTRIBUTION

In this dissertation the publications are original research papers on quantitative ultrasound imaging and finite difference modelling of ultrasound propagation in articular cartilage and agarose scaffolds containing collagen or chondrocytes. In all papers, the author participated in study design.

In paper **I**, the author carried out the ultrasound measurements and data analysis and was the main writer of the manuscript.

In paper **II**, the author carried out the ultrasound measurements and Fourier transform infrared imaging, conducted the data analysis and was the main writer of the manuscript.

In paper **III**, the author conducted the numerical modelling and analysis and was the main writer of the manuscript.

In paper **IV**, the author helped in sample collection, conducted 250-MHz scanning acoustic microscopy measurements and data-analysis, conducted the light microscopy imaging and analysis, and contributed analysing the 50-MHz scanning acoustic microscopy data. The author was co-writer in paper **IV** having made an equal contribution with D. Rohrbach.

In all studies, the contribution of co-authors has been significant.

TABLE OF CONTENTS

ABBREVIATIONS

2D	Two-dimensional
3D	Three-dimensional
BEM	Boundary element method
CND	Cell number density
DFS	Depth frequency spectrum
FDTD	Finite difference time domain
FEM	Finite element method
FTIR	Fourier transform infrared
GAG	Glycosaminoglycan
ICRS	International Cartilage Repair Society
IVUS	Intravascular ultrasound
LM	Light microscopy
MMP	Matrix degradation protein
MRI	Magnetic resonance imaging
OA	Osteoarthritis
OCT	Optical coherence tomography
PG	Proteoglycan
PLM	Polarized light microscopy
PZT	Lead zirconate titanate
PVDF	Polyvinylidene difluoride
QUS	Quantitative ultrasound
RF	Radio-frequency
ROI	Region of interest
SAM	Scanning acoustic microscopy
SD	Standard deviation
TOF	Time-of-flight

SYMBOLS

A	Peak to peak amplitude
$A(z_v, f)$	Frequency and depth dependent attenuation function
AFB	Apparent frequency dependence of backscatter
AIB	Apparent integrated backscattering
α_a	Classical absorption coefficient
$\alpha(\omega)$	Attenuation coefficient
α_{amp}	Amplitude attenuation
α_{int}	Integrated attenuation
$\boldsymbol{C}$	Stiffness tensor
c	Wave velocity
c_L	Longitudinal speed of sound
C_p	Specific heat capacity
c_T	Transversal speed of sound
γ	Ratio of heat capacities
d	Space dimension, thickness
d_i	Distance between transducer
δ	Kronecker delta function
Δt	Time step
Δx	Spatial grid step
$E(f)$	Acoustoelectric system transfer function
$\boldsymbol{\epsilon}$	Elastic strain tensor
f	Frequency, Body force vector
$FFT\{...\}$	Fourier transform
$G(f)$	Acquisition system transfer function
H_s^2	Surface independent diffraction function
h	Thickness
I	Intensity
IL	Intensity level
IRC	Integrated reflection coefficient
K	Scattering vector magnitude, Bulk modulus
k	Wave number, Reflection amplitude
κ	Thermal conductivity
κ_0	Compressibility of homogeneous medium
λ	Wavelength, First Lamé parameter
μ	Backscattered energy, Second Lamé parameter
N_c	Number of aligned cell layers
$\boldsymbol{\eta}$	Viscosity tensor
ω	Angular velocity
p	Pressure
P_n	Legendre polynomial
ϕ	Phase
ϕ_u	Unwrapped phase
$\Phi(\boldsymbol{K})$	Angle distribution factor
ϕ_0	Density of homogeneous medium

R	Reflection coefficient
ρ	Density
S_c	Reflected signal
$\mathrm{S_c}$	Cell layer spacing
SOS	Speed of sound
σ	Scattering cross-section
$\sigma_b(\omega), BSC$	Backscatter coefficient
T	Time period
$\boldsymbol{T}$	Stress tensor
$T_c(z, f)$	Transmission coefficient
θ	Angle
u	Displacement vector
URI	Ultrasound roughness index
V	Volume
V_c	Deviation of cells from alignment
Z	Acoustic impedance
$\langle ... \rangle$	Average operator
$\nabla \cdot$	Divergence operator
∇^2	Laplace operator

1 Introduction

Osteoarthritis (OA) is a common degenerative joint disease, occurring commonly in knee, hip and metacarpal joints. The prevalence of OA increases due to increasing obesity and aging of population [1–3]. Furthermore, it has been estimated that every third person over the age of 45 suffers from OA symptoms varying from occasional joint stiffness to permanent immobilization and severe pain [4]. OA represents an enormous economic burden to society [5,6] and it has been estimated that in Finland, OA is reponsible for annual costs of 1 billion € [7]. This is mainly due to expensive medical treatments such as joint replacement surgeries and early retirements [8]. Furthermore, OA has a major effect on an individual's life affecting functional and social activities, relationships and emotional well-being [9,10].

The integrity of cartilage structure is critical for the proper functioning of the joint. In early OA, the collagen network starts to degenerate and the water content of tissue increases, this being manifested as cartilage swelling and furthermore, the stiffness of subchondral bone increases [11,12]. Chondrocytes, *i.e.* the cartilage cells, try to maintain tissue structure by synthetizing proteins and macromolecules [13,14]. However, if the chondrocytes fail to maintain tissue homeostasis, then the tissue starts to degenerate [4,15]. These degenerative changes in the cartilage structure exert a great impact on the mechanical properties and durability and can ultimately lead to a complete loss of the tissue.

Even though cartilage repair techniques have advanced, there is still no cure for OA and current medication aims at the alleviation of OA symptoms [16,17]. Due to the weak regenerative capability and relatively low cell number density of articular cartilage, OA usually continues to progress over time. However, if the disease is detected in its early stage progression, OA may be slowed down or even stopped by decreasing OA related risk factors such as obesity [18,19].

Currently, radiographic imaging and magnetic resonance imaging (MRI) are two major techniques used in clinical practice to diagnose OA [20,21]. However, the radiographic image cannot reveal early OA changes and only the late signs of physical wear can be observed as a narrowed joint space. Current advanced MRI methods can provide more structural and quantitative information about the cartilage and the surrounding tissues [22,23]. However, MRI is a relatively costly imaging modality often plagued by prolonged patient queues and long acquisition times may be needed in order to quantify the matrix changes (*e.g.* by means of relaxation time mapping) [24,25]. After the findings from radiography or MRI have been evaluated, the patient can be recommended to undergo arthroscopy where an orthopaedic surgeon may attempt to repair cartilage injuries. During arthroscopy, the cartilage and other soft tissues are evaluated both visually and by probing with an arthroscopic hook. These methods do not provide information about the tissue's inner properties or the subchondral bone. Therefore, quantitative diagnostic methods would be beneficial in the evaluation of cartilage during arthroscopy.

Ultrasound imaging has demonstrated potential in the evaluation of articular cartilage during arthroscopy [26–29]. Moreover, transcutaneous ultrasound imaging has been claimed to be useful in the diagnosis of knee OA [30–32]. Quantitative

ultrasound methods can provide a comprehensive assessment of articular cartilage from the measurement of surface roughness as well as an evaluation of cartilage's inner structure and even subchondral bone [33–36]. In addition, in comparison with optical methods such as optical coherence tomography, an ultrasonic wave can penetrate further into the tissue, providing an estimation of cartilage thickness [26,37]. However, more information on how the structural components of articular cartilage affect ultrasound propagation is required for the optimization of this technique and thus for the further development of quantitative ultrasound techniques.

This thesis investigates ultrasound backscatter from articular cartilage and its structural components by using experimental and computational methods. Studies **I** and **II** were experimental investigations on ultrasound backscattering from chondrocytes and collagen, and examining the anisotropy of ultrasound backscattering in articular cartilage. A clinical intravascular ultrasound imaging device suitable for arthroscopic use was applied in studies **I** and **II**. In study **III**, the finite difference time domain (FDTD) method was used to simulate ultrasound wave scattering from chondrocytes and collagen in a similar setup as applied in study **I**. In study **IV**, experimental 50-MHz scanning acoustic microscopy (SAM) and computational FDTD methods were applied to investigate the coherent backscatter arising from human cartilage chondrocytes. Furthermore, 250-MHz SAM was applied in the characterization of the mechanical properties of the chondrocytes and the extracellular matrix.

2 Articular cartilage

There are three different types of cartilage in the human body: elastic cartilage, fibrocartilage and hyaline cartilage. Elastic cartilage is present in ear and epiglottis [38]. Fibrocartilage can be found in the intervertebral disks and meniscus [38,39]. Joint surfaces are coated with hyaline cartilage. Hyaline cartilage, also known as articular cartilage is transparent, has a highly organized structure and it does not contain nerves or blood vessels [40]. The main functions of articular cartilage are to distribute the load evenly in a joint and to provide nearly frictionless movement of the joint [40,41].

2.1 STRUCTURE AND COMPOSITION

The main components of articular cartilage are water, collagen, proteoglycans and chondrocytes which all have an organized structure in the tissue. Hyaline cartilage has a high water content and collagen and proteoglycans account for approximately one third of the wet weight of the tissue (Table 2.1).

Table 2.1: Proportions of cartilage constituents [40,42,43].

Collagen (ww%)	Proteoglycan (ww%)	Water (ww%)	Chondrocytes (vf%)
10–22%	4–7%	60–80%	1–5%

ww% = wet weight, vf% = volume fraction.

2.1.1 Collagen

Most of dry weight (60–80%) of cartilage consists of collagen [40]. Collagen is a protein which has a significant role in forming the cartilage structure and conferring its special mechanical characteristics. Type II collagen is the most abundant form, representing more than 90% of the collagens in cartilage [40]. Other collagen types present in cartilage are types III, VI, IX, X, XI, XII and XIV [44,45]. Together with type II collagen fibrils, they contribute to the stabilization of the collagen network [44,46]. All of the above mentioned collagen types have a triple helix structure of three polypeptide chains [44,46]. Collagen molecules of types IX and XI form cross-links with other collagen types in the fibril network [47,48], which stabilizes the collagen network and increases the tensile properties of the tissue [49,50].

Collagen forms a highly organized fibril network in the tissue [40,51,52]. The size of the collagen fibrils varies according to the fibril diameter, ranging from 20 nm up to 200 nm [40,53]. Cartilage can be divided into three depth-wise different zones based on the orientation of collagen fibrils (the Benninghoff model): superficial, transitional and deep zones (Figure 2.1). In the superficial zone (0–200 m), collagen fibrils are thinner (25–50 nm [53]) and oriented in parallel to the articular surface. In the transitional zone, fibrils are thicker (60–140 nm [53]) and they are randomly

oriented. In the deep zone, one finds the thickest fibrils (up to 160 nm [53]) and these form thick bundles of collagen fibers (∼55 µm) which are oriented in perpendicular to the articular surface [54]. Calcified cartilage is located underneath the deep zone; its function is to anchor the articular cartilage to the underlying subchondral bone [47].

2.1.2 Proteoglycan

Proteoglycans (PGs) are macromolecules which are embedded in the collagen network. In all, 4–7% of the wet weight and 25–35% of dry weight of cartilage consist of PGs. PGs have a specific role in the cartilage mechanics, since these are the molecules responsible for the tissue's osmotic swelling properties.

PGs contain glycosaminoglycan (GAG) chains [55]. GAG chains are composed of chondroitin sulphate and keratan sulphate which are negatively charged [55]. A PG monomer contains a GAG chain attached to a hyaluronan chain and an aggregate is formed when multiple PG monomers are connected to the hyaluronan chain [56]. Although there are several different PGs present in the articular cartilage, the most abundant PGs in cartilage are the large aggregating (50–85%) and non-aggregating types (10–40%) [40]. The GAG chains have a negative charge and they attract positive ions (*e.g.* Na^+) therefore giving rise to the osmotic pressure [57] which provides cartilage with its ability to resist compressive loads [58]. The collagen network binds PGs in the extracellular matrix. However, GAG chains are mobile and can be forced closer together. This increases the internal charge density as a way of balancing the compressive forces [56]. In healthy cartilage, the PG concentration is lower in the superficial zone and increases towards the cartilage-bone interface [47].

2.1.3 Chondrocytes

Chondrocytes, *i.e.* cartilage cells, account for only 1–5% of the tissue volume [40, 43]. Chondrocytes are long-living cells; their main function is to maintain and organize the tissue structure in the avascular, low oxygen environment, metabolizing glucose by glycolysis [59]. The mean diameter of a chondrocyte is ∼13 µm [43]. The organization and shapes of chondrocytes vary in the different cartilage layers (Figure 2.1) [60, 61]. In the superficial zone, the chondrocytes are isolated, ellipsoid and smaller than those in the deep zone. The cell density is highest in the superficial zone [43]. In the transitional zone, the cells are more round and they can be arranged in groups of two to three cells. In the deep zone, chondrocytes are arranged in depth-wise columns containing multiple cells. [43, 61]

Chondrocytes are surrounded with a pericellular matrix and together they form a unit called the chondron [62]. The pericellular matrix, which contains collagen types II, VI and IX and has a high PG content, acts as an interface between the chondrocytes and the surrounding extracellular matrix [62, 63].

The metabolic activity of a chondrocyte is affected by the mechanical stresses to which it is exposed [64]. Moreover, changes in the cartilage structure and extracellular matrix composition *e.g.* due to degeneration, affect the response and the morphology of the chondrocytes [47, 65].

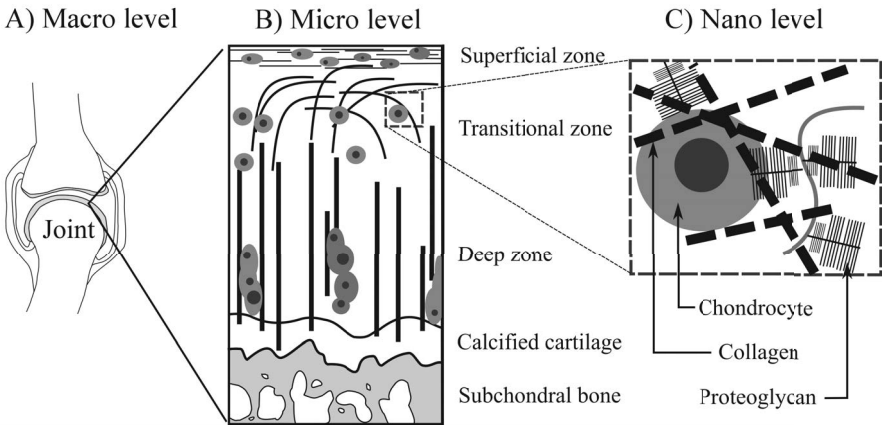

Figure 2.1: Illustration of the macro (A), micro (B) and nano level (C) structure of articular cartilage. The depth-dependent collagen network and chondrocyte structures are presented in detail in the micro level image.

2.2 OSTEOARTHRITIS

Osteoarthritis (OA) is a slowly progressing disease, characterized by degeneration of articular cartilage and sclerosis and remodeling of subchondral bone. OA can be classified into primary or secondary OA depending on its cause [66]. In primary OA, the cause of is not known [67]. However, in secondary OA, the disease is attributable to a known factor *e.g.* joint injury, inflammation, metabolic disorders or mechanical overloading of the joint [67]. OA caused by an injury is also called post-traumatic OA. The most common risk factors causing OA are age, obesity, gender, lack of exercise or excessive loading of the joint [2,68].

2.2.1 Symptoms of OA and related changes in articular cartilage

OA is often asymptomatic. The most common symptoms are pain, stiffness and swelling of the joint [67]. Since cartilage is an aneural tissue, the pain occurs usually in the late stage of the disease when cartilage has worn off and the subchondral bone which contains nerve endings is exposed to direct mechanical contact.

In addition to hyaline cartilage, OA also affects the surrounding tissues. Degeneration of the meniscus and changes in the subchondral bone are common. Inflammation is usually present in OA and the synovial fluid contains inflammatory substances. Due to avoidance of the use of the painful joint, muscle weakness may occur, which can lead to changes in the normal motion range of the joint [4,69].

The early stage of OA is characterized by the fibrillation and the disorganization of the collagen network and the loss of large aggregating PGs. This increases the permeability and water content of the tissue and decreases the stiffness of the tissue [4, 11,70]. In addition, in the very early stage of the disease, alterations in the subchondral bone as well as an increase in the thickness of the subchondral plate may occur [11]. In early OA, chondrocytes try to repair the tissue by synthetizing PGs and collagen. Unfortunately, the low cell density and the lack of vascularization mean that this tissue has a limited capability to regenerate or repair itself [71]. There are changes in

cell morphology and the cell density may even increase due to cell proliferation. In the hyperthophic repair phase, cell homeostasis becomes disrupted and the cells start to release proinflammatory cytokines [72,73]. After the early repair stage, chondrocytes start to synthetize and release matrix metalloproteinases (MMPs) which causes a continuous loss of cartilage tissue [11].

In most cases, the repair processes fail to prevent the tissue degeneration and the disease progresses to its late stage. The typical sign of the late stage is the gradual loss of cartilage matrix due to the inability of chondrocytes to synthesize collagen and proteoglycans; this is observed as visible signs of fibrillation on the articular surface. Moreover, cell cloning may occur and chondrocytes can form cell clusters [67]. Spontaneous repair cartilage (fibrous cartilage) may be formed and bone remodelling occurs in the subchondral bone due to the increased mechanical load. Finally, cartilage wears off totally, exposing the underlying subchondral bone [67].

2.2.2 Treatment

Currently, no cure exists for OA and medication is mainly used to relieve the pain and control the inflammation in joints by using analgesics (*e.g.* paracetamol and codeine), or anti-inflammatory drugs (*e.g.* ibuprofen) [74]. Pain control and the maintenance of the joint function are the most important goals in the treatment of OA. Furthermore, by reducing the common risk factors, the progression and symptoms of OA can be minimized. Therapeutic exercising, training the supporting muscles and weight loss have been shown to slow down OA progression [75].

Surgical methods such as microfracturing techniques [76], osteochondral auto- or allografts [77], autologous chondrocyte transplantation [78] and osteotomy [79] have been introduced to repair cartilage injuries or to slow down the progression of OA [67]. If cartilage wears off completely, a full or partial joint replacement surgery is the final option. This is an expensive operation and there are severe risk factors inherent in the implant surgery *e.g.* body can reject the implant and re-surgeries might be necessary if the implantation operation fails.

2.2.3 Diagnostics

Diagnosis of OA begins with the palpation of the joint and surrounding tissues. Commonly, radiographic imaging is the next step. Radiographic images can reveal osteophytes and narrowing of the joint space which is usually a sign of late stage of the disease. Magnetic resonance imaging (MRI) may be conducted if an injury in cartilage, menisci or the ligaments is suspected. MRI provides much better soft tissue contrast than conventional X-ray imaging. However, the spatial resolution of MRI images is limited which may limit its ability to detect the early stage degenerative changes and localized injuries. [80]

Conventional arthroscopy is a minimally invasive operation but it can be advantageous *e.g.* in ligament or cartilage injury repair. During arthroscopy, the articular surfaces can be evaluated both visually and by mechanical probing. For example, cartilage injuries can be graded using an International Cartilage Repair Society (ICRS) scoring system in which the cartilage lesion severity is classified into five categories [81]. The weakness of the different scoring systems is that they are subjective and the inter-observer reliability of the arthroscopic grading of cartilage lesions is poor [82,83]. Moreover, in conventional arthroscopy, only the properties of

the articular surface can be evaluated. Cartilage thickness, relative lesion depth or possible degeneration of the subsurface structures cannot be quantified.

Conventional arthroscopy may be enhanced by supplementing the procedure with quantitative imaging. For example, optical coherence tomography (OCT) can provide detailed information on the lesion size and shape [84] and could therefore make lesion scoring more reliable [85]. Moreover, OCT has the potential to be able to quantify the cartilage structure [86]. Ultrasound arthroscopy has been applied in knee and shoulder joints [26,29]. With quantitative ultrasound imaging, the roughness of the cartilage surface can be estimated and furthermore, the quantitative parameters derived from the backscattered signal can be advantageous in the evaluation of the subsurface cartilage matrix [34,87]. Low ultrasound frequencies ($\leq$10 MHz) can penetrate through cartilage and into subchondral bone and this makes it possible to measure cartilage thickness and evaluate the integrity of subchondral bone [29,88].

3 Ultrasound

By definition, ultrasound is a mechanical wave which has a frequency above the range of human hearing (>20 kHz). Ultrasound waves can be classified into three different types depending on how the wave oscillates. Transverse or shear waves oscillate perpendicularly to the wave propagation direction and they are present only in solid materials. Longitudinal or compressional waves oscillate along the direction of propagation and are present in gasses, plasma, liquids and solids. A surface wave is a combination of shear and longitudinal waves and propagates along the interface between two different media (liquid or solid), however, its use in biomedical ultrasound is minimal. Moreover, biological tissues are typically modelled as liquids in the field of biomedical ultrasound, because soft tissues have a high water content.

The basic relationship between wave propagation velocity (c), frequency (f) and wavelength (λ) is

$$c = f\lambda, \tag{3.1}$$

where $f = 1/T$ where T is the time period for one oscillation. The frequency range used in diagnostic ultrasound applications varies from the kilohertz range to tens of megahertz [89]. However, in research applications *e.g.* in scanning acoustic microscopy, the frequencies can reach into the gigahertz range [89].

3.1 ELASTODYNAMIC WAVE EQUATION

Acoustics is a field of physics which studies time varying deformations, usually oscillations, in a medium [90]. Matter is constructed of atoms which can be forced into a vibrational motion about their equilibrium positions. However, in continuum mechanics, it is assumed that small material particles or infinitely small volumes still consist of multiple atoms and therefore, molecular dynamics *e.g.* molecular vibrations and translations are ignored.

The translational equation of motion for a vibrating medium can be derived from Newton's second law [90]:

$$\rho \frac{\partial^2 \boldsymbol{u}}{\partial t^2} - \nabla \cdot \boldsymbol{T} = \boldsymbol{f}, \tag{3.2}$$

where ρ is density, $\boldsymbol{u}$ is the displacement vector, $\boldsymbol{T}$ is the stress tensor, t is time, $\boldsymbol{f}$ is the body force vector and $\nabla\cdot$ is the divergence operator.

Hooke's law states that for small deformations, the strain in a deformed body is linearly proportional to the applied stress and vice versa [90]. Hooke's law can be written as

$$T_{ij} = \sum_{k=1}^{d} \sum_{l=1}^{d} C_{ijkl} \epsilon_{kl}, \tag{3.3}$$

where $\boldsymbol{C}$ is the symmetric stiffness tensor and $\boldsymbol{\epsilon}$ is the elastic strain tensor. Furthermore, Hooke's law for an isotropic material can be expressed in a simplified form

$$T_{ij} = \lambda \delta_{ij} \epsilon_{k,k} + 2\mu \epsilon_{ij}, \tag{3.4}$$

where λ and μ are the Lamé parameters.

Elastic strain tensor is defined as

$$\epsilon_{ij} = \frac{1}{2}\left(\frac{\partial u_i}{\partial x_j} + \frac{\partial u_j}{\partial x_i}\right) \quad \text{for } i, j = 1, 2, 3. \tag{3.5}$$

Now, we can substitute eq. (3.4) into eq. (3.2), set the body force ($\boldsymbol{f}$) to zero (freely vibrating media) and finally, obtain the wave equation of motion for an isotropic elastic medium in a vector form

$$\rho\frac{\partial^2 \boldsymbol{u}}{\partial t^2} - \mu\nabla^2\boldsymbol{u} = (\lambda + \mu)\nabla(\nabla \cdot \boldsymbol{u}), \tag{3.6}$$

where ∇^2 is $\nabla \cdot \nabla$ *i.e.* the Laplace operator.

The above equation can be simplified using the Helmholtz decomposition ($\boldsymbol{u} = \nabla\Phi + \nabla \times \boldsymbol{H}, \nabla \cdot \boldsymbol{H} = 0$):

$$\nabla\left[(\lambda + 2\mu)\nabla^2\Phi - \rho\frac{\partial^2\Phi}{\partial t^2}\right] + \nabla \times \left[\mu\nabla^2\boldsymbol{H} - \rho\frac{\partial^2\boldsymbol{H}}{\partial t^2}\right] = 0, \tag{3.7}$$

where Φ and $\boldsymbol{H}$ are scalar and vector potentials, respectively. This equation is valid only when both terms vanish which leads to the following wave equations for compressional and transversal wave motions:

$$\nabla^2\Phi = \frac{1}{c_L^2}\frac{\partial^2\Phi}{\partial t^2}, \tag{3.8}$$

and

$$\nabla^2\boldsymbol{H} = \frac{1}{c_T^2}\frac{\partial^2\boldsymbol{H}}{\partial t^2}, \tag{3.9}$$

where $c_L = \sqrt{\frac{\lambda+2\mu}{\rho}}$, and $c_T = \sqrt{\frac{\mu}{\rho}}$, are the speed of sound for compressional and transversal waves, respectively. [91]

For quiescent homogeneous fluid media, the equilibrium parameters (ρ_0, p_0, $\mathbf{u_0} = 0$) are subjected to a disturbance which is characterized as a perturbation of the equilibrium state [92]:

$$\begin{aligned} \rho &= \rho_0 + \delta\rho. \\ p &= p_0 + \delta p. \\ \mathbf{u} &= \delta\mathbf{u}. \end{aligned} \tag{3.10}$$

Now, inserting these into the equation of continuity for mass, Euler's equations for the conservation of momentum and equation of state for density, pressure and displacement, the linear wave equation where the second order terms are neglected is as follows:

$$\nabla^2 p - \frac{1}{c^2}\frac{\partial^2 p}{\partial t^2} = 0, \tag{3.11}$$

where p is the pressure on the fluid medium, and $c = \sqrt{\frac{1}{\rho_0\kappa_0}}$ is the propagation speed in a lossless medium where κ_0 is the compressibility of the medium [92].

In order to describe the wave equation for inhomogeneous (scattering) fluid media, the density term must be changed by adding the inhomogeneities *i.e.* fluctuations ($\delta\rho_e$) in the medium as follows:

$$\rho = \rho_0 + \delta\rho_e + \delta\rho. \tag{3.12}$$

Now, the acoustic wave equation takes the form [92]

$$\nabla^2 p - c^2 \frac{\partial^2 p}{\partial t^2} = \gamma_\kappa(\boldsymbol{r}) \frac{1}{c^2} + \nabla \cdot (\gamma_\rho(\boldsymbol{r}) \nabla p), \tag{3.13}$$

where

$$\gamma_\kappa(\boldsymbol{r}) = \frac{\kappa_e(\boldsymbol{r}) - \kappa_0}{\kappa_0}$$
$$\gamma_\rho(\boldsymbol{r}) = \frac{\rho_e(\boldsymbol{r}) - \rho_0}{\rho_e}. \tag{3.14}$$

The terms on the right side of the eq. (3.13) are known as scattering sources [92].

3.1.1 Plane and spherical waves

The harmonic single frequency plane and spherical waves are common types of waves applied in acoustics. They can be expressed as

$$p = P_0 e^{i(\boldsymbol{k}\cdot\boldsymbol{r} - \omega t)}, \tag{3.15}$$

where $\boldsymbol{k}$ is the wave vector, $\boldsymbol{r}$ is the radial distance, P_0 is constant for a plane wave and $P_0 = \frac{P_0}{r}$ for a spherical wave, respectively. When equation (3.15) is substituted into the wave equation (eq. 3.11), then the dispersion relation can be found

$$\omega = \pm c|k|. \tag{3.16}$$

For both plane and spherical waves, it can be shown that the acoustic intensity is [93]

$$I = \frac{|p|^2}{2\rho_0 c}. \tag{3.17}$$

Sound intensity is usually expressed on a logarithmic scale since the sound intensity has great variability. Audible sound wave intensities can range from 10^{-12} to 10 $\mathrm{W/m^2}$ [93]. Therefore, it is beneficial to describe the sound levels on a decibel (dB) scale and the intensity level (IL) is defined as

$$\mathrm{IL} = 10 \log\left(\frac{I}{I_{\mathrm{ref}}}\right), \tag{3.18}$$

where I_{ref} is the reference intensity [93].

3.2 REFRACTION, REFLECTION AND SCATTERING

When an acoustic wave propagates through an interface between two media having different acoustic impedances, it can reflect, refract and transmit. There are no discontinuities in particle velocity or pressure when a wave propagates and therefore when a wave encounters an interface between two different materials, the particle velocity and pressure are continuous across the boundary. This assumption is satisfied when incident pressure p_i is equal to transmitted p_t and reflected pressures p_r

$$p_i = p_r + p_t, \tag{3.19}$$

and similarly for particle velocities:

$$v_i \cos\theta_i - v_r \cos\theta_r = v_t \cos\theta_t. \tag{3.20}$$

From these two equations and assuming that $p = \rho c v$, the intensity reflectance $\frac{I_r}{I_i}$ and intensity transmittivity $\frac{I_t}{I_i}$ can be determined [89]:

$$\frac{I_r}{I_i} = \left(\frac{Z_2 \cos\theta_i - Z_1 \cos\theta_t}{Z_2 \cos\theta_i + Z_1 \cos\theta_t} \right)^2, \tag{3.21}$$

$$\frac{I_t}{I_i} = \frac{4 Z_2 Z_1 \cos\theta_i \cos\theta_t}{\left(Z_2 \cos\theta_i + Z_1 \cos\theta_t\right)^2}. \tag{3.22}$$

Specular reflection occurs when the surface is smooth and diffuse reflection occurs when the interface is rough. If the object size is smaller than or equal with the wavelength, then the wave scatters from the object [89].

Snell's law states that when a wave enters into a medium with different acoustic impedance the direction of the wave propagation will change according to the relationship:

$$\frac{\sin\theta_i}{c_i} = \frac{\sin\theta_t}{c_t}, \tag{3.23}$$

where θ_i and θ_t are the angles of the arriving and refracted waves with respect to the surface normal and c_i and c_t are the velocities of the incident and refracted waves, respectively. If $c_2 < c_1$ the direction of the propagation moves towards the boundary normal. In addition to reflection and refraction, the wave will change its direction when it passes through a barrier with an opening. This phenomenon is known as diffraction. If the size of the obstacle or barrier is similar to the wavelength of the wave, the diffraction effect is more intense.

3.2.1 Wave scattering in inhomogeneous media

Scattering occurs when an incident ultrasound wave encounters heterogeneity in the medium. Scattering interactions in tissues may be characterized by the scattering cross-section σ [92]. Scattering interactions may be categorized into three different groups based on the object size [89]: with an object size larger than the wavelength $\sigma = 1$ *i.e.* specular scattering, with an object size similar to the wavelength *i.e.* diffractive scattering and with an object size smaller than the wavelength $\sigma \propto k^4 a^6$, where a is the radius of the scatterer and k is the wavenumber *i.e.* diffusive scattering (Rayleigh scattering) [89].

Macroscopic level dissimilarities such as variations in density and compressibility within the tissue structure cause scattering in biological tissues [92]. Scattering is frequency dependent such that scattering increases with increasing frequency. There are two popular theoretical methods that are used for the analysis of the ultrasound scattering. The first method involves investigating wave scattering from a single scatterer. The following solution by Faran (1951) for the pressure field (p_s) in the far field is valid for a rigid spherical scatterer [94]:

$$|p_s| \xrightarrow[r\to\infty]{} \frac{P_0}{kr} \left| \sum_{n=0}^{\infty} (2n+1) \sin(\eta_n) \exp(i\eta_n) P_n(\cos\theta) \right|, \tag{3.24}$$

where P_0 is the pressure amplitude of the incident wave, k is the wavenumber, r is the radius of the scattering sphere, n is the order of the solution (integer), $j = (-1)^{1/2}$, η_n is the scattering phase angle, P_n is the Legendre polynomial and θ is the scatter angle. Calculation of η_n is rather cumbersome and is not considered here. Readers are referred to the paper by Faran (1951) to see the full solution [94].

The second, even more general method, is to use the Green's function approach. In this method, a scattering source function is added to the wave equation (eq. 3.13) [92, 95]. Usually, wave scattering is investigated by assuming the tissue to be fluid (shear modulus = 0 in the tissue). The scattered pressure field can be expressed as a function of the angle distribution factor ($\Phi(\boldsymbol{K})$):

$$p_s(\boldsymbol{r}) = \frac{Pe^{ikr}}{r}\Phi(\boldsymbol{K}), \tag{3.25}$$

where $\Phi(\boldsymbol{K})$ is

$$\Phi(\boldsymbol{K}) = \frac{k^2}{4\pi}\int_V \gamma(\boldsymbol{r_0}, \Theta)e^{-i\boldsymbol{K}\cdot\boldsymbol{r}_0}dv_0. \tag{3.26}$$

By fixing the scattering angle *e.g.* at $\Theta = 180^\circ$ the scattering medium can be theoretically characterized by a single function $\gamma(\boldsymbol{r})$ [92].

Scattering cross-sections (σ_s) are relevant measures in the characterization of the scattering interactions in the tissues. The differential scattering cross-section (σ_{ds}) is defined as

$$\sigma_{ds} = \frac{d\sigma_s}{d\Omega}, \tag{3.27}$$

where σ_s is the scattering cross-section and Ω is the solid angle. For scattered incident plane wave σ_{ds} can be written as

$$\sigma_{ds} = |\Phi(\boldsymbol{K})|^2, \tag{3.28}$$

where $\boldsymbol{K}$ is the scattering vector ($\boldsymbol{K} = 2k\sin\Theta/2$) [92].

Differential backscattering cross-section per unit volume also known as the backscatter coefficient (BSC, unit $\mathrm{cm}^{-1}\mathrm{sr}^{-1}$) can be expressed as:

$$\mathrm{BSC} = |\Phi(2\mathrm{k})|^2/\mathrm{V}, \tag{3.29}$$

where V is the volume of the medium that participates in generating the differential power [92].

One experimental method of determining the BSC is to use the reference phantom technique [96]. If the BSC of the reference material and attenuation in the sample and reference material are known, BSC of the sample can be determined with the following equation:

$$\sigma_b(\omega) = \sigma_b^R(\omega)e^{-4z(\alpha_S(\omega))}\frac{|S_S(\omega)|^2}{|S_R(\omega)|^2}, \tag{3.30}$$

where z is depth, $\sigma_b(\omega)$ is the BSC of the sample, $\alpha_S(\omega)$ is the attenuation coefficient of the sample, $\sigma_b^R(\omega)$ is the BSC of the reference material and $\alpha_R(\omega)$ is the attenuation coefficient of the reference sample [96]. Several experimental methods for determining the BSC are presented in the book written by Mamou and Oelze [95]. With the knowledge of BSC coefficient, it is possible to extract information about the properties of the scatterer such as its diameter and density, which can be related to tissue structure and possible pathologies.

3.2.2 Absorption

Absorption is a process where vibrational energy is converted into heat [97]. This conversion can be divided into three different types: heat conduction losses, viscous losses and losses caused by internal molecular processes [93, 97]. Heat conduction losses occur via the conduction of thermal energy when there are high and low temperature rarefactions in the medium [93]. If there are relative motions between portions of the medium, viscous losses will occur. Soft tissues have a high liquid content and viscous absorption can be taken into account for viscous fluids by adding a Kelvin-Voigt model into the generalized Hooke's law as follows:

$$T_{ij} = c_{ijkl}\epsilon_{kl} + \eta_{ijkl}\frac{\partial \epsilon_{kl}}{\partial t}, \tag{3.31}$$

where η is the viscosity tensor [90].

The classical absorption coefficient α_a is the sum of viscous and thermal absorption coefficients

$$\alpha_a = \frac{\omega^2}{2\rho_0 c^3}\Big(\frac{4}{3}\eta + \frac{(\gamma-1)\kappa}{c_P}\Big), \tag{3.32}$$

where ω is the angular velocity, ρ_0 is the medium density, η is the medium viscosity, γ ratio of heat capacities, κ is thermal conductivity, c_P is the specific heat at constant pressure [93]. The classic absorption equation does not take into account the absorption due to the molecular processes.

3.2.3 Attenuation

Ultrasonic waves attenuate in biological tissues. The phenomena which cause wave attenuation are absorption and scattering and the geometrical divergence of the wave when it propagates further away from the source. Absorption is the dominant factor that contributes to the attenuation in soft tissues. The power law describes ultrasonic wave attenuation and it takes the form

$$p(x) = pe^{-\alpha(\omega)\Delta x}, \tag{3.33}$$

where $\alpha(\omega) = b\omega^m$ [89]. Coefficients b and m are experimentally determined for the material. Attenuation is frequency dependent such that high frequencies are attenuated more than those at the lower frequencies.

3.3 ULTRASOUND IMAGING OF ARTICULAR CARTILAGE

This section describes the generation of ultrasound and summarizes the main ultrasound techniques used for the imaging of articular cartilage.

3.3.1 Ultrasound generation

When voltage is applied to the sides of a piezoelectric solid material *e.g.* lead zirconate titanate (PZT), its dimension will change. This phenomenon is called electrostriction. The reverse of this phenomenon is called a piezoelectric effect, which means that when mechanical stress is applied to a material, a potential difference between the sides of the material is generated. The ultrasound transducer works according to these phenomena such that transmitting ultrasound transducer converts the electrical signal

into a mechanical wave and the receiving transducer converts an arriving mechanical ultrasound wave to an electrical signal. The same transducer can transmit and receive ultrasound signals. PZT is the most common material used in transducer elements but polyvinylidene difluoride (PVDF) and its co-polymers can also be used [98]. Compared with PZT, PVDF has a lower acoustic impedance, a more flexible structure and it can transmit ultrasound pulses with broader bandwidths [98].

3.3.2 Transcutaneous ultrasound

In transcutaneous ultrasound imaging, an array transducer is applied and coupled with gel to the surface of the skin. This method has been used for the clinical evaluation of articular cartilage, meniscus and subchondral bone in the knee joint [30, 99, 100]. Furthermore, this technique is commonly applied in the imaging of metacarpal-phalangeal joints [101, 102]. Transcutaneous ultrasound mainly gives structural information about cartilage *e.g.,* its thickness [37]. It has been reported that transcutaneous ultrasound imaging does have the potential to be used as a screening tool for OA and synovitis at the primary health care level [31, 32, 99, 103].

In the recent study of Koski *et al.* 2016, ultrasound imaging was compared with conventional radiography when imaging the knee osteophytes from femoral medial and lateral bone margins [32]. The intra- and inter-reader agreements were compared between ultrasound and radiography images of the knee and it was shown that the ultrasound was as good as radiography in terms of reliability and reproducibility for detecting the presence of osteophytes [32].

The advantages of the transcutaneous ultrasound technique are that it is widely available in hospitals, imaging costs are low and the investigation is safe for the patient. However, there are also a few related disadvantages. The main limitation is the inability to visualize the whole articular surface, due to the limited acoustic window. In addition, the experience of the sonographer affects the outcome and currently there are no fully standardized or validated grading methods for the ultrasound evaluation of the joint space narrowing. [99]

3.3.3 Ultrasound arthroscopy

Ultrasound imaging can be applied during arthroscopy by applying a small ultrasound transducer inside the joint through an arthroscopic portal [26, 29, 104–106]. This minimally invasive technique provides quantitative information about the tissue structure. An intravascular ultrasound (IVUS) device, originally designed for the imaging of myocardium and coronary arteries, has been exploited during arthroscopic surgeries [26,29,88,107]. The IVUS catheter consists of a small piezoelectric transducer element which rotates inside the catheter producing a live cross-sectional image. Ultrasound arthroscopies have already been conducted in human knee, hip and shoulder joints *in vivo* [26, 29, 104, 105, 108]. This technique enables the visualization of the whole articular surface and estimation of the cartilage properties by enabling the determination of quantitative ultrasound parameters for the evaluation of cartilage surface and subchondral bone [26, 29, 109]. The limiting factor in ultrasound arthroscopy is that the ultrasound transducer can be applied only to the largest joints having enough space to insert the transducer (diam. 1–3 mm) between the joint surfaces. Furthermore, to acquire quantitative data, ultrasound pulse incidence should be perpendicular to the articular surface which can be difficult to achieve in clinical arthroscopy [110].

3.3.4 Acoustic microscopy

A scanning acoustic microscope (SAM) can be used to estimate the acoustic and elastic properties of materials and tissues [87, 111–115]. Typically, a focused sound beam is used in pulse-echo geometry and in SAM either the transducer or the sample is moved in *x-y* -directions to scan the sample. The scanning plane and the sample surface should be parallel, which may be challenging to achieve with cartilage samples with curved surfaces [116]. The scan resolution is usually a trade-off between penetration depth and resolution. With higher frequency transducers, the spatial resolution is improved due to the smaller beam diameter at focus, but the high frequency waves attenuate more rapidly, limiting the penetration depth. Ultrasound frequencies applied in SAM of articular cartilage vary from tens to even thousands of megahertz [36, 117, 118]. Lower frequency ultrasound (<10 MHz) enables the visualization of the subchondral bone [36], whereas high frequency SAM can be used for the quantitative evaluation of the articular surface where the signs of early OA occur, such as collagen network fibrillation [33, 114, 119, 120].

3.4 QUANTITATIVE ULTRASOUND EVALUATION OF ARTICULAR CARTILAGE

Quantitative ultrasound parameters have been introduced in the evaluation of articular cartilage (table 3.1) [121]. These techniques investigate changes in the roughness and reflection of the articular surface, ultrasound speed, attenuation and analysis of the backscatter spectrum.

Fibrillation and roughening of articular surface decreases ultrasound surface reflection [107, 114, 119, 122]. The reflected ultrasound pulse can be evaluated in both the time (reflection coefficient, *R*) and frequency domains (integrated reflection coefficient, *IRC* [34]) (table 3.1). In addition, surface roughness can be quantified with the ultrasound roughness index (*URI*, table 3.1) which calculates the root mean square value of the roughness [122, 123]. These surface reflection based parameters can be used to distinguish between mechanically degraded [28], repaired [124] and osteoarthritic cartilage [33] from normal cartilage.

Cartilage subsurface structures can be evaluated by analyzing the backscatter signal [26, 34, 87, 109, 125]. Ultrasound backscatter has been found to increase in the presence of repair cartilage [125, 126] and a decrease in cases of osteoarthritic cartilage [26, 109]. Both the collagen fiber network and the chondrocytes have been shown to have an effect on the ultrasound backscatter [34, 87, 126]. Chérin *et al.*, 1998 introduced along with *IRC* the apparent integrated backscatter (*AIB*) parameter (table 3.1) [34]. *AIB* is evaluated from the scatter signal in the frequency domain. Scattering from the cartilage inner structures can be modelled in the frequency domain as follows:

$$S_c(z_v, f) = E(f) \times G(f) \times A(z_v, f) \times H_v^2(z_v, f) \times T_c^2(z, f) \times U(z_v, f), \qquad (3.34)$$

where z_v is the distance of the volume dV from the transducer, $T_c^2(z, f)$ is the frequency dependence of the double transmission coefficient for the cartilage surface, $U(z_v, f)$ is the backscattering function including all scatterers in the volume dV, $H_v^2(z_v, f)$ is the volume-integrated diffraction function and $A(z_v, f)$ is the total attenuation in the media. *AIB* can be obtained by normalizing the scatter spectrum of the sample with the reflection spectrum from the perfect reflector to remove the acquisition system characteristics and diffraction influences (table 3.1).

Table 3.1: Typical quantitative ultrasound parameters for the evaluation of the articular cartilage [34, 87, 122, 127–133].

Parameter	Equation
Ultrasound roughness index (µm)	$URI = \sqrt{\frac{1}{n}\sum_{i=1}^{n}(d_i - \langle d \rangle)^2}$
Reflection coefficient (%)	$R_c = \frac{A_c}{A_{ref}} \cdot 100\%$
Speed of sound (m/s)	$SOS = \frac{2h}{TOF}$
Amplitude attenuation (dB/mm)	$\alpha_{\text{amp}} = \frac{10}{h}\log_{10}\frac{A_1}{A_2}$
Integrated attenuation (dB/mm)	$\alpha_{\text{int}} = \frac{1}{\Delta f}\int_{\Delta f}\frac{10}{h}\log_{10}\frac{A_1(f)}{A_2(f)}$
Integrated reflection coefficient (dB)	$IRC = \frac{1}{\Delta f}\int_{\Delta f} 20\log_{10}\frac{S_c(z,f)}{S_{ref}(z,f)}\text{df}$
Apparent integrated backscatter (dB)	$AIB = \frac{1}{\Delta f}\int_{\Delta f} 20\log_{10}\frac{S_c(z,f)}{S_{ref}(z,f)}\text{df}$

n = number of the scan lines, d_i = distance between the transducer and articular surface in the i^{th} scan line, and $\langle d \rangle$ = average distance from the transducer to the surface. A_c = peak to peak amplitude of the reflection from the cartilage surface, A_{ref} = peak to peak amplitude of the reflection from a perfect reflector. h = cartilage thickness, TOF = time-of-flight. Δf = -6-dB frequency band, A_1 = first reflection echo from cartilage-metal interface where cartilage is attached, A_2 = second reflection echo from cartilage-metal interface. $S_c(z,f)$ = reflection/backscatter signal in frequency domain of the sample, $S_{ref}(z,f)$ = reflection signal in frequency domain from perfect reflector.

The length of the gate window and the delay where the scatter signal is acquired can be adjusted and depth-dependent scattering can be evaluated by using a sliding window and calculating *AIB* in a depth-wise manner [87]. Within the -6-dB bandwidth of the spectrum, a linear regression analysis can be performed. The slope of the linear fit is the apparent frequency dependence of backscatter (*AFB*) [87]. In addition to Fourier transform based spectrum analysis techniques, wavelet transforms have also been applied to ultrasound data for the investigation of the spectrum versus time or depth plots [104, 134, 135]. From the transformed data the maximum magnitude and echo duration can be evaluated. For OA cartilage, the maximum magnitude decreases and the echo duration increases [135].

The relationship between the speed of sound (*SOS*) and articular cartilage properties has been widely investigated [127–131]. *SOS* of articular cartilage is anisotropic [128], varies within the anatomical location (1579–1934 m/s [136–138]) and decreases in degenerated cartilage [127, 133]. When ultrasound propagates perpendicular to the articular surface, the *SOS* is higher in comparison with ultrasound propagation in parallel to the surface [128, 130] and *SOS* increases in conjuction with cartilage depth [130].

Ultrasound attenuation is related to the composition and structure of the cartilage and several methods have been developed for the estimation of the ultrasound attenuation of articular cartilage in both time and frequency domains (table 3.1) [132, 133]. Ultrasound attenuation in articular cartilage has been reported to be around 27.7–66.1 dB/cm in the frequency range of 10–40 MHz [132]. Furthermore, a significant correlation was found between histological integrity and ultrasound attenuation [133]. The literature values for the quantitative ultrasound parameters of articular cartilage are presented in table 3.2.

Table 3.2: Mean values of apparent integrated backscatter (*AIB*), apparent frequency dependence of backscatter (*AFB*), integrated reflection coefficient (*IRC*), reflection coefficient (*R*), ultrasound roughness index (*URI*), attenuation and speed of sound (*SOS*) of ultrasound in articular cartilage. Values without standard deviations are medians extracted from figures.

Species	Site	Status	*n*	*AIB* (dB)	*AFB* (dB/MHz)	*IRC* (dB)	*R* (%)	*URI* (µm)	Attenuation (dB/mm)	*SOS* (m/s)	*f* (MHz)	Study
Human	Femoral joint	Mankin I: 0	8	-	0.2	-35	-	2.5	-	-	40	[87,114]
		Mankin I: 1		-	-0.05	-38	-	10	-	-		
		Mankin I: 2	11	-	-0.03	-41	-	12.5	-	-		
		Mankin I: 3	13	-	-0.03	-45	-	13	-	-		
		Mankin I: 4	6	-	-0.03	-44	-	10	-	-		
Human	Knee arthroscopy	ICRS: 0	13	-44.7 ± 8.1	-	-30.7 ± 5.9	3.5 ± 2.3	11.5 ± 9.0	-	-	9	[109]
		ICRS: 1	23	-46.8 ± 5.8	-	-32.9 ± 4.0	2.5 ± 1.2	14.6 ± 11.2	-	-		
		ICRS: 2	14	-52.0 ± 6.7	-	-38.7 ± 3.3	1.2 ± 0.5	18.2 ± 9.8	-	-		
Human	PAT	Intact	16	-47.5	-	-	-	-	-	-	40.2	[139]
Ovine		Intact	10	-51.5	-	-	-	-	-	-		
Bovine		Intact	8	-48.2	-	-	-	-	-	-		
Human		Cross-section	16	-46	-	-	-	-	-	-		
Ovine		Cross-section	10	-40	-	-	-	-	-	-		
Bovine		Cross-section	8	-45.5	-	-	-	-	-	-		
Bovine	PAT	Intact	7	-61.0 ± 0.9	-	-25.4 ± 1.9	6.1 ± 1.2	10.7 ± 3.6	-	-	40	[28]
		Mechanically degradated	7	-61.1 ± 1.5	-	-33.4 ± 3.5	2.7 ± 1.4	25.6 ± 14.9	-	-		
Bovine	FE	Intact	7	-61.3 ± 1.0	-	-29.5 ± 3.6	4.1 ± 1.3	15.0 ± 6.2	-	-		
		Mechanically degradated	7	-61.2 ± 0.9	-	-36.0 ± 4.1	2.0 ± 0.9	24.5 ± 6.1	-	-		
Bovine	PAT	Control	20	-53.1 ± 2.7	-	-17.7 ± 4.3	-	6.0 ± 1.4	-	-	40	[120]
		Collagenase treated	20	-50.1 ± 3.2	-	-26 ± 6.8	-	42.1 ± 35.6	-	-		
		Control	20	-52.7 ± 2.0	-	-17.6 ± 4.6	-	5.9 ± 1.7	-	-		
		Trypsin treated	20	-51.2 ± 2.4	-	-14.6 ± 3.8	-	5.4 ± 1.7	-	-		
Bovine		Intact	8	-	-	-	-		2.65 ± 0.58		10.3	[133]
Human	FC	Normal, young	7	-	-	-	-		6.2 ± 0.4	1666* ± 16*	30	[140]
		Normal	24	-	-	-	-		7.1 ± 0.4*	1664 ± 7*		
		Papain	24	-	-	-	-		8.5 ± 0.5*	1642 ± 9*		
Bovine	FC	Normal	12	-	-	-	-		6.8 ± 1.2*	1642 ± 8*		
		Interleukin-1α	12	-	-	-	-		9.1 ± 1.0*	1631 ± 17*		
Bovine	FMC	Intact/healthy	6	-	-	-30.2	2.7	12.0	-	-	20	[123]
	LPG		6	-	-	-31.2	2.5	14.4 ± 4.0	-			
	MTP		6	-	-	-33.7 ± 2.1	1.6 ± 0.5	16.2 ± 4.0	-	-		
	PAT		12	-	-	-27.1 ± 3.3	4.7 ± 2.7	8.4 ± 3.0	-	-		

*Mean ± SEM (standard error of mean), PAT = patella, FE = femoral sulcus, FC = femoral condyle MTP = medial tibial plateau, LPG = lateral patello-femoral groove FMC = femoral medial condyle.

3.5 NUMERICAL MODELLING OF ULTRASONIC WAVE PROPAGATION

There are several numerical and semi-analytical methods for the modelling of ultrasound wave propagation in connective tissues [141–148]. For the investigation of ultrasonic wave propagation in articular cartilage, the finite-difference time-domain (FDTD) method can be applied [116]. In the FDTD method, the space and time domains are discretized and they form a space-time grid (Figure 5.1). The discretized wave equation is solved at the nodes in the FDTD method [142,149]. The finite-element method (FEM) is based on the discretization of space to mesh. FEM can be used for more complicated geometries, since the shape of elements is more flexible (triangular or polygon meshes) compared to the rectangular uniform grid applied in the FDTD methods. In the boundary element method (BEM), only a boundary is discretized. FEM and BEM solve integral forms of the wave equation [91]. In BEM, the volume integral forms are converted into surface integrals using Green's functions [91]. In addition to these methods, spectral and pseudo spectral methods can be applied in the numerical modelling of ultrasonic wave propagation [145,150].

In hybrid modelling, multiple numerical and/or analytical methods are used in one simulation by dividing the simulation domain into subdomains and using different methods in the different subdomains [146]. For example, wave propagation in complex geometry can be modelled by using the FDTD method and the propagation of the wave in the homogeneous medium *e.g.* water can be calculated semi-analytically [146]. Hybrid modelling can reduce the total computational time compared with a simulation conducted using a single method [146].

3.5.1 Finite difference time domain method

Finite difference methods solve differential equation such as wave equations by approximating the derivatives using finite differences. Wave propagation in linear elastic and isotropic medium can be described by elastodynamic equations. This method was first applied by Yee (1966) in the field of electromagnetics [151] and later to simulate seismic waves [152]. The FDTD method provides solutions for field values (speed and pressure) at discrete locations in space for different time instants. The spatial mesh in the time domain consists of a regular grid of field values which are then solved for time instants (Figure 5.1) [152].

The approximate finite difference (central difference) expression for the first-order derivative can be derived from the Taylor expansion

$$f'(a) = \frac{f(a + \frac{\Delta a}{2}) - f(a - \frac{\Delta a}{2})}{\Delta a}. \tag{3.35}$$

Moreover, from equation (3.35), the following second-order approximation for the second-order derivative can be determined

$$\frac{\partial^2 f}{a^2} = \frac{f(a + \Delta a) - 2f(a) + f(a - \Delta a)}{\Delta a^2}. \tag{3.36}$$

These centered difference approximations are then entered in to the wave equation as shown in the following example case for one dimensional wave equation.

Example of one dimensional wave equation for a lossless fluid

In a one dimensional case, velocity and stress can be formulated using the central difference approximation and the following form using Newton's second law (eq. 3.2) and Hooke's law (eq. 3.4) [149]:

$$\frac{p(x,\, t+\Delta t) - p(x,\, t)}{\Delta t} = -\lambda(x)\Big(\frac{v_x(x+\frac{\Delta x}{2},\, t+\frac{\Delta t}{2}) - v_x(x-\frac{\Delta x}{2},\, t+\frac{\Delta t}{2})}{\Delta x}\Big) \quad (3.37)$$

and

$$\frac{v_x(x,\, t+\Delta t) - v_x(x,\, t)}{\Delta t} = -\frac{1}{\rho(x)}\Big(\frac{p(x+\frac{\Delta x}{2},\, t+\frac{\Delta t}{2}) - p(x-\frac{\Delta x}{2},\, t+\frac{\Delta t}{2})}{\Delta x}\Big) \quad (3.38)$$

Now, from these explicit forms $p(x, t+\Delta t)$ and $v_x(x, t+\Delta t)$ can be solved when the velocity and pressure fields are known for the previous space and time instances [149]. In figure 5.1, staggered grids of pressure and velocity are shown for a two-dimensional case. This method can be applied also for solids by applying the constitutive relations to all stress components.

The FDTD method solves the wave equation only in a bounded region of the space. In ultrasound applications, the boundary is usually modelled as an unbounded medium, such as an absorbing boundary or as an interface of perfectly matched layers [153].

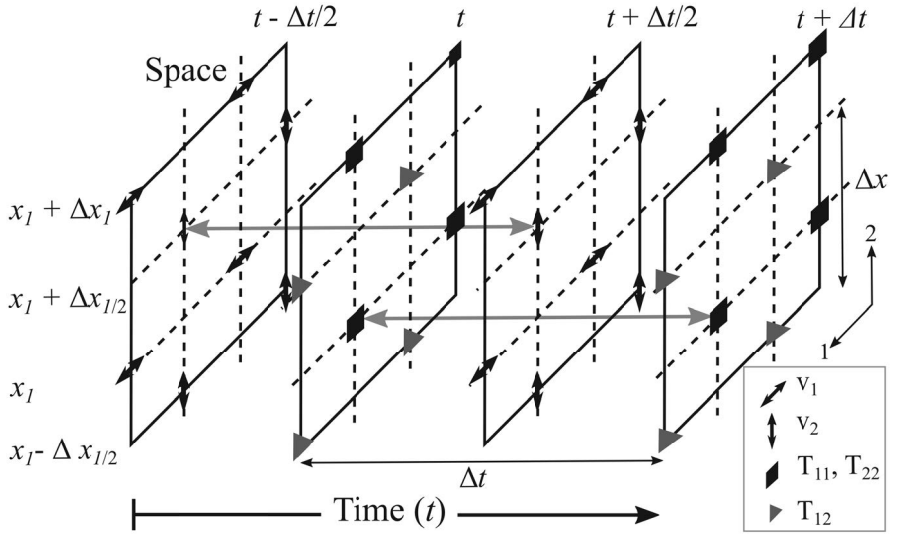

Figure 3.1: Illustration of grids for velocity v and stress tensor T in two dimensions. They are staggered in space and time [152].

The main advantage of the FDTD method is that it can handle solid-solid and liquid-liquid couplings as well as solid-liquid coupling between two different materials [149]. Furthermore, complex geometries can be modelled by digitizing the desired geometry *e.g.,* cortical bone [142, 143, 154]. The main disadvantage is the computational cost which increases drastically when the grid density increases. Moreover, originally smooth geometries are described by rectangular uniform grids, which can induce staircase artefacts into the model. Other disadvantages are the numerical dispersion and cumulative errors when simulations require a prolonged duration and a long ultrasound propagation distance. [149]

4 Aims of the present study

Quantitative ultrasound is a potentially useful tool for the investigation of the degeneration of articular cartilage. However, the contributions of different cartilage components such as chondrocytes and collagen on ultrasound backscattering are not fully understood. To fill this gap in knowledge, this thesis work has investigated these issues by applying experimental and computational methods. These advances could help in the optimization of ultrasound techniques for the diagnostic characterization of articular cartilage.

The aims of this thesis are to:

1. Determine the contribution of collagen and chondrocytes on the ultrasound backscatter by conducting ultrasound measurements with agarose hydrogel scaffolds containing varying concentrations of collagen and chondrocytes.
2. Investigate the anisotropy of the ultrasound backscatter in bovine articular cartilage.
3. Evaluate the suitability of FDTD modelling in the simulation of ultrasound propagation and scattering in articular cartilage by constructing models incorporating different concentrations of chondrocytes and collagen.
4. Estimate the acoustic impedance, speed of sound, density and bulk modulus of chondrocytes and the surrounding extracellular matrix using a high frequency SAM.
5. Investigate numerically and experimentally if chondrocyte spacing leads to coherence in ultrasound backscatter in human articular cartilage and further, to examine whether this exerts any effect on apparent integrated backscatter and the apparent frequency dependence of the backscatter.

5 Materials and methods

This thesis consists of four studies **(I-IV)** utilizing the materials and methods summarized in table 5.1.

Table 5.1: Summary of the materials and methods used in the studies **I-IV**.

Study	Sample material	n	Methods
I	Chondrocytes prepared in agarose	7 cell number densities n = 9/cell number density	Ultrasound imaging Light microscopy FTIR
	Collagen prepared in agarose	8 concentrations n = 9/concentration	
II	Bovine articular cartilage samples	11	Ultrasound imaging Light microscopy Polarized light microscopy FTIR imaging
III	Collagen in agarose Chondrocytes in agarose	9 concentrations 7 cell densities	FDTD modelling
IV	Human articular cartilage samples	9 samples 3 sections 9 sections	50-MHz SAM 250-MHz SAM Light microscopy
	Cell spacing models	10 realizations of each set: N_c = [2, 3, 4, 5] µm V_c = [0, 2, 4, 6, 8] µm S_c = [15, 20, 25, 30, 35, 40] µm	FDTD-modelling
	Random cell distribution models	10 realizations of each set: CMA = [8, 10, 12, 14, 15, 18, 20] µm CND = [12, 14, 36, 48, 60]$\times 10^3 \frac{\text{cells}}{\text{mm}^3}$	FDTD-modelling

SAM = scanning acoustic microscopy, FTIR = Fourier transform infrared imaging, N_c = number of aligned cell layers, V_c = deviation from perfect cell alignment, S_c = cell layer spacing, CMA = cell minor axis, CND = cell number density.

5.1 SAMPLE PREPARATION

In study **I**, collagen and chondrocytes were prepared in 4% agarose gel scaffolds. Agarose scaffolds with different collagen concentrations (0, 1.5625, 3.125, 6.25, 12.5, 25, 50 and 100 mg/mL) or different chondrocyte number densities (0, 1, 2, 4, 8, 16, 32 million cells/mL) were prepared. Nine scaffolds with each concentration or each cell number density were prepared. The collagen concentration in human articular cartilage is close to 200 mg/mL [155], however due to difficulties preparing collagen in agarose scaffolds, the highest possible concentration prepared was 100 mg/mL. Chondrocyte number densities were selected to cover the range of cell number density in human articular cartilage ($\sim$14 million cells/mL).

In the preparation of collagen scaffolds, 100 mg of type I collagen (calf skin, Sigma-Aldrich, St. Louis, MO,USA) was dissolved in 1 mL of 0.1 M hydrochloric acid. Next, the solution was diluted in 8% low-melting agarose gel at 40°C (NuSieve GTG agarose low melting, Cambrex Bio Science, Rockland, ME, USA) to achieve the desired collagen concentrations in agarose which was present at concentration of 4%.

Additionally, nine agarose scaffolds with 100 mg/mL collagen concentration were made by dissolving 200 mg/mL of collagen in 1 mL of 0.1 M HCl and diluting in 8 % agarose. In order to construct scaffolds with chondrocytes, cartilage was harvested from bovine femoral condyles and chondrocytes were isolated. Finally, 64, 32, 16, 8, 4, 2, 0 million cells/mL were mixed in the 8% agarose gel to obtain the required cell concentrations with an agarose concentration of 4%. The agarose gel suspensions were pipetted into cylindrical wells (diam. = 5.9 mm and height = 3.9 mm) and a glass sheet was pressed on the surface to make it perfectly flat.

In study **II**, eleven bovine knee joints were collected from a local abattoir (HK Ruokatalo Oy, Outokumpu, Finland). Visually intact patellas (n = 11) were extracted from the knee joints and cylindrical samples (diam. = 29 mm) were prepared from the medial side. Subsequently, the osteochondral samples were split into halves using a razor blade (0.009" 2-facet steel-back single-edge blade, Personna American Safety Razor, Verona, VA, USA). Finally, ultrasound measurements were conducted through the intact articular surface and the cut side.

In study **IV**, a total of nine osteochondral samples were collected from both knee joints of two human cadavers (male: 67 years n = 4, female: 51 years, n = 5). The samples were prepared from lateral femoral condyle, medial tibial plateau and upper lateral quadrant of the patella. Kuopio University Hospital ethical committee reviewed the sample collection protocol (favourable opinion: 58/2013). After the 50-MHz SAM measurements, samples were fixed in formalin and embedded in paraffin and three 10 µm thick sections were used for 250-MHz SAM.

5.2 ULTRASOUND IMAGING METHODS

Studies **I-II** were conducted with an intravascular ultrasound (IVUS) system using 40-MHz and 9-MHz ultrasound transducers. Both transducers have been used in our previous clinical studies [26,29]. The 40-MHz ultrasound provides higher resolution images and it is more sensitive to backscatter. However, 9-MHz ultrasound has been shown to propagate through the whole cartilage tissue, enabling an estimation of the cartilage thickness [29].

In study **IV**, 50-MHz and 250-MHz scanning acoustic microscopes were used. The 50-MHz ultrasound transducer had a broad bandwidth suitable for cell spacing estimation and 250-MHz ultrasound was selected since it provided high resolution quantitative maps, making possible an estimation of mechanical properties of the chondrocytes.

5.2.1 Intravascular ultrasound

IVUS device (ClearView Ultra, Boston Scientific, San Jose, CA, USA) with catheters having a rotating 9 MHz (Ø= 2.8 mm, -6 dB bandwidth = 7.1–11.0 MHz) and 40 MHz (Ø= 1 mm, -6 dB bandwidth = 30.1–45.3 MHz) ultrasound transducers were used in studies **I** and **II** (Figure 5.1). Ultrasound signals were recorded and digitized with the 250 MHz sampling rate and at a resolution of 8 bits using a digital oscilloscope (Teledyne LeCroy, Chestnut Ridge, NY, USA). With a custom made LabVIEW software (Version 8.2, National Instruments, Austin, TX, USA) data from ten full rotations were stored with the measurements being repeated three times. The ultrasound incidence angle at the articular surface was adjusted manually with a goniometer for each measurement such that maximum surface reflection was obtained.

5.2.2 Scanning acoustic microscopy

In study **IV**, 50-MHz and 250-MHz SAMs were used for the quantitative ultrasound imaging of *ex vivo* human articular cartilage samples and fixed human cartilage sections, respectively. In the 50-MHz measurements, the fresh samples were immersed in 36°C PBS and measured with a SAM200Ex device [156]. Scan increments in the x- and y-directions were 40 µm. The 50 MHz transducer was spherically focused and made of polyvinylidene fluoride (PVDF) (KSI-PT50, center frequency 42 MHz, -6 dB bandwidth = 27–55 MHz, Krämer Scientific Instruments GmbH, Herborn, Germany). The width of the -6-dB beam in the focal plane was 88 µm and the depth of field was 2.7 mm.

Before conducting the 250-MHz SAM measurements, paraffin was removed from samples and cartilage sections were rehydrated using a series of HistoclearII (Electron Microscopy Sciences, Hatfield, PA, USA), ethanol (100%, 75%) and saline solutions (each 2 × 5 min). A custom-made 250-MHz SAM [157] system was used with 2 µm scanning increments in the x- and y-directions (Figure 5.1). A 300-MHz monocycle pulser (GZ1120ME-03, GEOZONDAS, Vilnius, Lithuania) was used to excite the focused 250-MHz transducer (center frequency 264 MHz, -6 dB bandwidth = 180–340 MHz, Fraunhofer IMBT, St. Ingbert, Germany). -6-dB beam width was 7 µm and the depth of field was 72 µm.

The radiofrequency signals were amplified (MITEQ, Hauppauge, NY, USA) and digitized at 2.5 GHz using a 12-bit oscilloscope (Teledyne LeCroy, Chestnut Ridge, NY, USA). The sample slide was set to be perpendicular to the ultrasound beam and deionized water was used as a coupling medium between the transducer and the section.

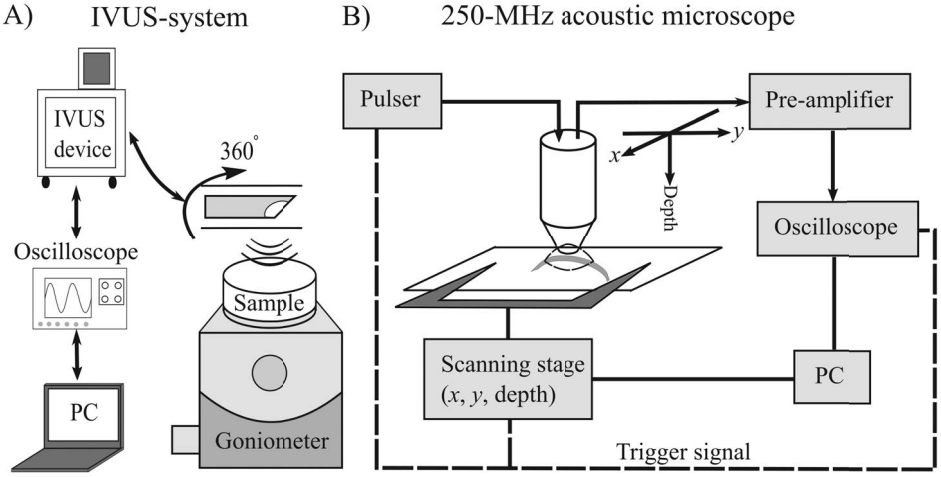

Figure 5.1: Geometries for A) IVUS measurements and B) for 250-MHz SAM measurements.

5.3 FDTD SIMULATIONS

An open source software SimSonic (www.simsonic.fr [142]) was used in studies **III** and **IV** to generate two dimensional (2D) FDTD models. A sine-Gaussian input signal with the center frequency of 40 MHz (-6 dB range: 27–53 MHz, study **III**) and a pulse with the center frequency of 45 MHz (-6 dB range: 36–54 MHz, study **IV**) were used as inputs. Source arrays were unfocused and a pulse-echo geometry was used in both studies. In study **III**, receivers were also placed in the top and bottom of the material to determine the speed of sound. In study **III**, attenuation was neglected whereas in study **IV**, frequency independent attenuation was taken into account [158]. In both studies, perfectly matched layers were used as boundary conditions to avoid reflections from the outer edges of the simulation domain [153].

In study **III**, rectangular spatial grid step (Δx) was 66.7 nm and 166.6 nm for the collagen and chondrocyte models, respectively. In study **IV**, the grid step was 1 µm. The time step (Δt) was selected in both studies such that the Courant-Friedrichs-Lewy condition was fulfilled, *i.e.*,

$$\Delta t \leq \frac{1}{\sqrt{d}} \cdot \frac{\Delta x}{c_{\max}}, \tag{5.1}$$

where d (= 2) is the dimension of the model and c_{max} is the highest speed of sound in the simulation.

The material parameters used in the simulations are summarized in table 5.2. In study **III**, material parameters were obtained from the literature, whereas in study **IV** parameters for extracellular matrix and chondrocytes were obtained from the 250-MHz SAM measurements. The attenuation for the extracellular matrix was obtained from the literature [140] and attenuation within chondrocytes was set to two times the value of water.

Table 5.2: Material parameters used in the studies **III** and **IV**. In study **III** attenuation was neglected while in study **IV** attenuation was included in the model.

Study	Material	Density (g/cm^3)	$C_{11} = C_{22}$ (GPa)	$C_{12} = C_{21}$ (GPa)	C_{44} (GPa)	Attenuation (dB/mm)
III	Water	1.000	2.241	2.241	0.00	-
	Agarose	1.058	2.163	2.163	0.00	-
	Collagen	1.350	7.487	7.487	0.000017	-
	Chondrocyte	1.050	2.241	2.241	0.00	-
	Nucleus	1.580	3.410	3.410	0.00	-
IV	Water	1.00	2.25	2.25	0.00	0.28
	Extracellular matrix	1.10	2.80	2.80	0.00	10.65
	Chondrocyte	1.04	2.56	2.56	0.00	0.56

In study **III**, simulation geometries were constructed to mimic the experimental geometries applied in study **I**. Collagen models had collagen concentrations of 1.5625, 3.125, 6.25, 12.5, 25, 50, 100 and 200 mg/mL. The final collagen concentration *i.e.* 200 mg/mL is in the range of typical collagen concentration of articular cartilage [155] and was included into the simulations. The chondrocyte models had cell number densities of 1, 2, 4, 8, 16 and 32 million cells/ml. The cells had a circular shape with a radius of 5 µm with the nucleus placed in the center of the cell having the radius of 2.5 µm. Collagen volume fractions were estimated from the concentrations assuming a collagen density of 1.35 g/cm^3 [159]. The collagen fibrils had random

positions and orientations and their thickness and length were 66.7 nm and 333.5 nm, respectively. Collagen and chondrocytes were generated in the model iteratively. Iteration continued until the area fraction in the domain was equal or higher than the set volume fraction. Moreover, two models with collagen concentrations of 100 mg/ml were designed to allow the fibrils to run through the agarose scaffolds in a direction either parallel or perpendicular to the surface.

In study **IV**, cells were modelled in a such that they were different in the superficial and deep zones. Superficial zone cells were modelled as ellipses with a 14 µm major axis parallel to the articular surface and with a 10 µm minor axis. Deep zone cells had a circular shape with a diameter of 14 µm. In the superficial zone, the cells were placed on a layered structure parallel to the surface. The depth-wise position of a chondrocyte in the layer was randomly altered by $\pm$ 2 µm. In the deep zone, chondrocytes were arranged into vertical columns consisting of 2–4 cells the positions of which were randomly altered in both the lateral and depth-wise directions by $\pm$ 5 µm and $\pm$ 7 µm, respectively. Furthermore, the spacing of the cell columns was set to randomly vary between 20–30 µm. The cell number densities were set to $24{\cdot}10^3$ cells/mm^3 and $8{\cdot}10^3$ cells/mm^3 for superficial and deep zones, respectively. The 2D cell number density (CND_{2D}) was estimated using the relationship $CND_{2D} = CND_{3D}^{2/3}$.

In order to investigate the effects of the distribution of chondrocytes in the superficial zone on the ultrasound backscatter, three sets of artificial cartilage models with layered structures were generated and the number of aligned cell layers (N_c), deviation of cells from the perfect cell alignment (V_c) and the cell layer spacing (S_c) were varied. The parameters were varied as: N_c = 2, 3, 4, 5, 6; V_c = 0, 2, 4, 6, 8; µm, and S_c = 15, 20, 25, 30, 35, 40 µm. Only one parameter was varied at one time and three realizations were generated, while the remaining parameters were kept constant *i.e.*, N_c = 6, V_c = $\pm$ 2 µm and S_c = 20 µm.

In addition, two sets of cartilage models with randomly distributed chondrocytes were created to study the influence of the cell size and cell number density on the ultrasound backscatter. In the first set, the dimensions of the cells varied from 4 µm to 28 µm with increments of 2 µm. The aspect ratios of the cells in the superficial and deep zones were 1.4 and 1, respectively. In the second set, the cell number density was varied from 6 $\cdot 10^3$ to 60 $\cdot 10^3$ cells/mm^3 in the superficial zone and simultaneously from 2 $\cdot 10^3$ to 20 $\cdot 10^3$ cells/mm^3 in the deep zone while the cell size was kept constant (14 µm major axis and 10 µm minor axis in the superficial zone, and 14 µm in diameter in the deep zone).

5.4 QUANTITATIVE ULTRASOUND PARAMETERS

Ultrasound image analysis

B-mode ultrasound images were analysed in studies **I** and **II** to evaluate the ultrasound backscatter from the agarose scaffolds containing collagen or chondrocytes and cartilage samples, respectively. First, the analysis window was positioned below the sample surface for the first frame and that position was used for the subsequent frames. An average image consisting of 30 subsequent frames was calculated. In studies **I** and **II**, the width of the analysis windows were 1 mm and 2.8 mm for 40-MHz and 9-MHz transducers, respectively. The depths of the windows were 4 mm and equal to cartilage thickness in studies **I** and **II**, respectively. Additionally, in study **II**, the length of the window was calculated based on the sound speed in the

parallel or perpendicular directions obtained from [130] to match cartilage thickness obtained from optical coherence tomography images.

In study **I**, a subtraction image between the average image of the scaffold containing collagen or chondrocytes and pure agarose was calculated to minimize the background noise and possible variation in the signal level between measurement sessions. Next, the average image was divided into ten equally sized depth zones and ultrasound backscatter was quantified as an average grayscale value for each zone separately. The grayscale value originally ranged from 0 to 255 and the values were linearly normalised to range from 0 to 1 to represent ultrasound backscattering in arbitrary units. Moreover, ultrasound backscatter representing the whole sample was determined by averaging zones 2 to 9. This was done in order to exclude reflections from the front and bottom ends of the sample. In addition in study **I**, the intensity histogram of 100 bins was determined for the average images to evaluate changes in the distribution of ultrasound backscattering intensity within the scaffold. In order to quantify the change in distribution, the skewness of the histogram was determined. The analysis of the ultrasound image was performed with Matlab R2012a (The MathWorks, Natick, MA, USA).

Apparent integrated backscatter

In studies **II** and **III**, apparent integrated backscatter (*AIB*) values were determined from the experimental and simulated data. *AIB* was calculated based on the equation shown in table 3.1. *AIB* calculation was performed with Matlab R2012a in both studies. In study **IV**, *AIB* was calculated from 50-MHz SAM measurements and simulations. Moreover, the apparent frequency dependence of backscatter (*AFB*) was determined within a -6-dB frequency bandwidth.

Speed of sound

In study **III**, simulated speed of sound was determined between the receivers located on the surface and on the bottom of the sample in the through transmission geometry. Hilbert envelope maximums were calculated for the surface and the bottom transducer signals and the 10% deviation of the Hilbert envelope maximum from the signal baseline was used as a threshold in the time-of-flight (TOF) determination. In addition, also the theoretical speed of sound values were calculated using a relation

$$SOS = \sqrt{\frac{K}{\rho}}, \tag{5.2}$$

where K and ρ are bulk modulus and density, respectively. For all collagen and chondrocyte concentrations, theoretical SOS was calculated as a weighted average using the volume fractions of agarose and collagen or chondrocytes.

In study **IV**, the speed of sound (c) values were determined from human cartilage sections measured with a 250-MHz SAM using the method described by Hozumi *et al.* 2004 [160]. In the study of Rohrbach *et al.* 2016 [161], the method is explained in detail and here only a short description of the calculation procedure is provided. When a cartilage section is measured in the pulse-echo geometry, reflections are observed from the water-sample interface ($s_1(t)$) and from the sample-glass plate interface ($s_2(t)$). The recorded RF signal can be modelled as a summation of these two signals ($s(t) = s_1(t) + s_2(t)$). Subsequently, the signals $s_1(t)$ and $s_2(t)$ can be

modelled as a phase shifted and amplitude modified versions of a reference signal $s_0(t)$ as

$$s_1(t) = ks_0(t - t_1),$$
$$s_2(t) = ms_0(t - t_2) * attn., \tag{5.3}$$

where k and m are the amplitudes of the recorded signals and t_1 and t_2 describe the shift in time of the two signals. $*attn.$ describes the attenuation effects due to wave propagation inside the sample section. The reference signal ($s_0(t - t_0)$) can be determined from the signal reflection from the water-glass interface. [161]

After the RF signals (s) are collected, they are transformed into the frequency domain and normalized with the reference signal. Taking the squared magnitude of this normalized spectrum yields

$$\left| \frac{FFT\{s_1 + s_2\}}{FFT\{s_0\}} \right|^2 = k^2 + 2km \cdot e^{-2df\alpha} \cdot \cos(2\pi f(t_2 - t_1)) + m^2 e^{-4df\alpha}, \tag{5.4}$$

where α is the attenuation coefficient, t_0 is the time of flight of the reference signal and f is frequency. If attenuation is neglected, the squared normalized spectrum reaches extremums at the frequencies f_{min} and f_{max} when a cosine function reaches extremums *i.e.:*

$$2\pi f_{min} \cdot (t_2 - t_1) = (2n + 1)\pi, \quad n \in \mathbb{N}_0 \tag{5.5}$$
$$2\pi f_{max} \cdot (t_2 - t_1) = 2n\pi, \quad n \in \mathbb{N}_0 \tag{5.6}$$

and the corresponding unwrapped phase angle ϕ_u of the magnitude spectrum at the f_{max} is [161]:

$$\phi_u = 2\pi f_{max}(t_0 - t_1) - 2\pi n. \tag{5.7}$$

Note that t_0 is the time of flight between the sample surface and glass plate in water and therefore:

$$\phi_u = 2\pi f_{max} \frac{2d}{c_0} - 2\pi n, \tag{5.8}$$

where c_0 is the speed of sound in the water and d is the section thickness.

The phase angle can be expressed as:

$$2\pi f_{max}(t_2 - t_1) = 2\pi f_{max}(t_0 - t_1) - \phi_u. \tag{5.9}$$

The thickness of the sample section can be solved as

$$d = \frac{\phi_u}{4\pi f_{max}\left(\frac{1}{c_0} - \frac{1}{\hat{c}}\right)}, \tag{5.10}$$

where $\hat{c}$ is the speed of sound in the specimen. Similarly for the minimum frequencies the thickness can be expressed as:

$$d = \frac{c_0}{4\pi f_{min}}\big(\phi_u + \pi(2n - 1)\big). \tag{5.11}$$

The f_{min} and f_{max} are frequencies which were detected using a peak detection algorithm and the n's can be determined from the estimated periodicity of f_{min} and f_{max}. From eq. (5.10) the speed of sound value can be solved for both f_{min} and f_{max}. Attenuation shifts the locations of the f_{min} and f_{max} which must be taken into account. By using eq. (5.4) the attenuation coefficient can be estimated. The detailed explanation of this correction procedure is provided in Rohrbach *et al.,* 2016 [161].

Acoustic impedance

In study **IV**, the acoustic impedance Z_c was determined with 250-MHz SAM using the following equation [161]:

$$Z_c = \frac{Z_w R_{ref} + \frac{k}{k_{ref}} Z_w}{R_{ref} - \frac{k}{k_{ref}}}, \tag{5.12}$$

where R_{ref} is the reflection coefficient of the reference signal:

$$R_{ref} = \frac{Z_{ref} - Z_w}{Z_{ref} + Z_w}, \tag{5.13}$$

and k and k_{ref} are the reflection amplitudes recorded at water–sample and water–glass interfaces, respectively. Z_w and Z_{ref} are the acoustic impedances of water and the glass plate, respectively. A custom-made Matlab software was used to obtain parameter maps of sample thickness (d), compressional wave velocity ($\hat{c}$), and acoustic impedance (Z).

Density and bulk modulus

After calculating the maps of speed of sound and acoustic impedance, then the density and bulk moduli maps of a sample could be derived using relations:

$$\rho = \frac{Z}{c}, \tag{5.14}$$

and

$$K = c \cdot Z. \tag{5.15}$$

The following thresholds were included for thickness, acoustic impedance and speed of sound to include only the reliable values in further analyses: 6–15 µm, 1–2 MRayl, and 1100–2000 m/s, respectively. The material properties for chondrocytes and extracellular matrix were estimated from a region of interest (ROI) of 0.5×0.5 mm^2 which was positioned in the center of the amplitude map. Cells were manually segmented from each ROI and the extracellular matrix was eroded with a disk shaped kernel (radius = 4 µm) to reduce the partial volume effect. Subsequently, mean values and standard deviations were calculated for cells and cartilage separately from the segmented maps (K, ρ, c and Z).

Depth dependent frequency spectrum and cell spacing estimation

In study **IV**, for both the 50-MHz SAM and simulations, a depth dependent frequency spectrum (DFS) was determined. Ultrasound signals were gated using a sliding hamming window. The overlap of the gates in the depth direction was 12.5 ns (*i.e.*, $\sim$10.3 µm). The log compressed power spectrum was determined for each gated signal from which the reference power spectrum was subtracted to obtain DFS($depth$, f), where f is the frequency in MHz and $depth$ is the position of the gate in mm.

For each $depth$ in the DFS the peak frequency (f_{pk}) was detected to estimate the cell layer spacing (Figure 5.2). A frequency peak was defined as a local extrema if the difference between its amplitude and its neighbouring local minima was larger than a set threshold of 0.1 dB. If more than one peak was detected, then the peak (f_{pk}^n)

closest to the center frequency of the reference signal was selected. Subsequently, spectra were normalized by the maximum amplitude of the DFS and all peaks below -10 dB were removed to exclude unreliable peaks. By assuming that the speed of sound value in cartilage (c) is 1590 m/s, f_{pk}^{n} was then converted to a spacing value using the following equation:

$$\text{Spacing} = \frac{nc}{2f_{pk}^{n}}. \tag{5.16}$$

Individual spacing values were defined to be outliers and removed from further analysis, if they were out of the interquartile range (*i.e.* smaller or larger than 25$^{\text{th}}$ or 75$^{\text{th}}$ percentiles [162] within each depth). Finally, spacing estimates were averaged between 100 µm and 250 µm depths with intervals of 25 µm, yielding 6 average spacing values per sample. Spacing estimates between cartilage surface and 100 µm depth were excluded because the signals were affected by the surface reflection.

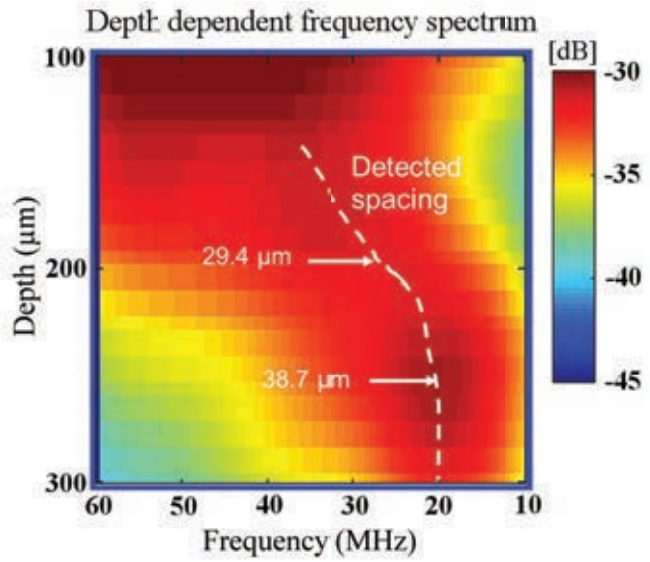

Figure 5.2: Example image of depth dependent frequency spectrum (DFS) and the corresponding detected cell spacing values.

5.5 REFERENCE METHODS

This section shortly summarizes the reference methods used in studies **I-IV**.

Optical coherence tomography

Optical coherence tomography (OCT) was applied in study **II** to measure the cartilage thickness. OCT images were acquired using Ilumien PCI Optimization System (St. Jude Medical, St. Paul, MN, USA) equipped with an OCT catheter (C7 Dragonfly, St. Jude Medical).

Light microscopy

In all studies, light microscopy was conducted using an Axio Imager M2 microscope (Carl Zeiss MicroImaging, Jena, Germany). In study **I**, one representative sample was randomly selected for light microscopy from each collagen and chondrocyte concentration. Three sections of scaffolds containing collagen were stained with Masson's trichrome and three sections of scaffolds containing chondrocytes were stained with Hematoxylin and Eosin and imaged by light microscopy.

In study **II**, the relative chondron area was estimated (in all samples) from sections stained with Safranin-O and imaged in a light microscope. ROI area of 1 mm $\times$ cartilage thickness was selected for analysis.

In study **IV**, the Mankin score was used to evaluate the degeneration of the samples such that three Safranin-O stained sections were scored by three investigators and their results were averaged and rounded to the nearest integer for each sample. Cell morphology for the numerical simulations was evaluated from the cells located between the articular surface those at a and depth of 250 µm. Cells were segmented manually from the light microscopy images and cell spacing was estimated from the images in the following way: Each segmented image was divided into overlapping rectangular ROIs (depth: 100 µm, width: 500 µm, overlap: 90%). Each depth column within each ROI was gated using Tukey window and power spectrum was calculated. Then average spectrum from all spectra within the ROI was calculated and log-compressed. The maximum peak frequency (f_{peak}) was determined and converted into a spacing value using the relation $\frac{dz}{f_{peak}}$, where dz is the pixel size and f_{peak} is the frequency of the peak. Spacing values were averaged in 25-µm intervals between 100-µm and 250-µm depths relative to the cartilage surface.

Fourier infrared imaging

In study **I**, three unstained sections of scaffolds containing collagen were imaged with an FTIR spectroscope (Spectrum Spotlight 300, Perkin Elmer, Shelton, CO USA) and integrated absorbance in the Amide I region (wavenumber range: 1600-1700 cm^{-1}) was used to determine the collagen concentration within the section [163].

In study **II**, three non-stained cartilage sections from each sample were imaged with a Fourier transform infrared spectroscope (Spectrum Spotlight 300). Spectral and pixel resolutions of the FTIR system were 4 cm^{-1} and 25 µm, respectively. Integrated absorbance in the Amide I region (wavenumber range: 1585-1720 cm^{-1}) was used to evaluate the collagen concentration as a function of cartilage depth [163].

Polarized light microscopy and digital densitometry

In study **II**, collagen fiber orientation was estimated with polarized light microscopy. The regions of interest were selected to be 1 mm $\times$ cartilage thickness. The depth-wise orientation and the parallelism index of collagen network were then calculated for each sample [164]. In study **II**, The spatial PG distribution (Safranin-O stained cartilage section) was determined with digital densitometry [165].

5.6 STATISTICAL ANALYSES

In all studies, the limit of statistical significance was set to $p = 0.05$. In study **I**, Kruskal-Wallis test was used to test if the difference in backscattering and the skewness of the ultrasound intensity distribution between different concentrations of cells or collagen were statistically significant. In study **II**, Wilcoxon signed rank test was used to determine the significance of differences in ultrasound backscatter between measurements through the articular surface and lateral (cut) surface. In addition, Spearman's ρ was calculated to evaluate correlations between ultrasound backscatter parameters and collagen orientation or concentration. In studies **I** and **II**, SPSS software was used for statistical analyses (SPSS V. 19, Chicago, IL, USA). In study **IV**, Kruskal-Wallis tests with post-hoc Bonferroni correction were used to test sample-specific (Mankin score) and modality-related (light microscopy and 50-MHz SAM) differences in cell spacing estimates. Moreover, Pearson correlation was used to evaluate the relationship between cell-spacing and depth and correlations between 50-MHz SAM parameters and LM based cell spacing. All statistical tests in study **IV** were performed using the Statistics Toolbox of Matlab R2014a (Mathworks, Natick, MA, USA).

6 Results

6.1 ULTRASOUND BACKSCATTER FROM CHONDROCYTES

6.1.1 Effect of cell number density on ultrasound backscatter

In study **I**, ultrasound (9 and 40 MHz) backscatter increased significantly ($p < 0.05$) when the cell number density (CND) increased in the agarose scaffolds (Figure 6.1). Furthermore, the skewness of the distribution of ultrasound backscattering intensity differed significantly ($p < 0.05$) between scaffolds with different CND (Figure 6.1).

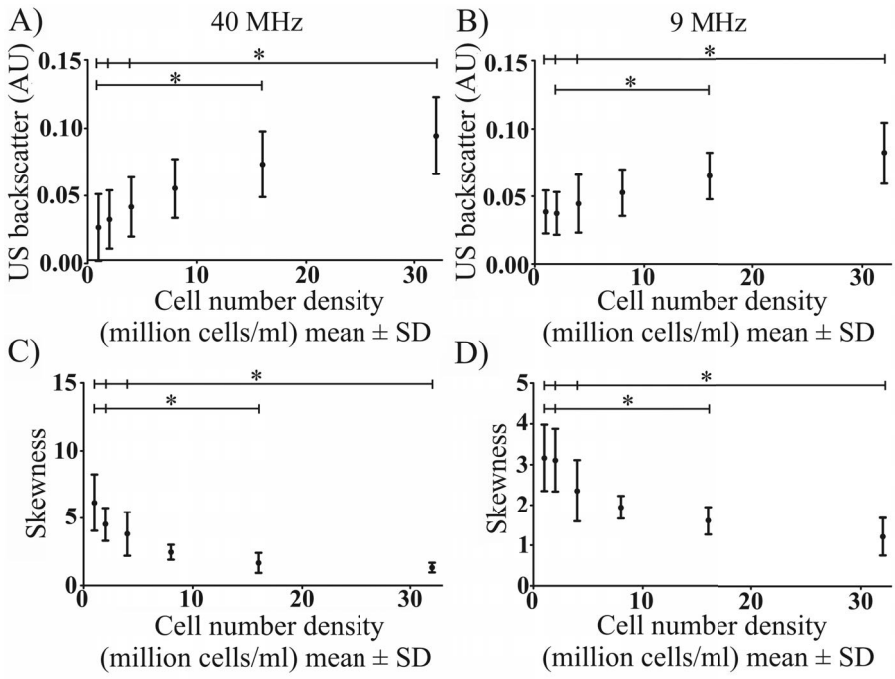

Figure 6.1: 40-MHz (A) and 9-MHz (B) ultrasound backscatter (arbitrary units, (AU)) as a function of cell number density. Skewness of the intensity distribution as a function of cell number density for 40-MHz (C) and 9-MHz (D) ultrasound. Standard deviations are marked with the error bars. *$p < 0.05$

With all cell number densities, an attenuation induced decrease in backscattering (at 40 MHz) along the cartilage depth was detected (Figure 6.2). Moreover, the rate of decrease in the backscattering elevated as CND increased. With 9-MHz ultrasound, no depth dependence on the backscatter was observed, indication of the relatively lower sensitivity of 9-MHz ultrasound on CND.

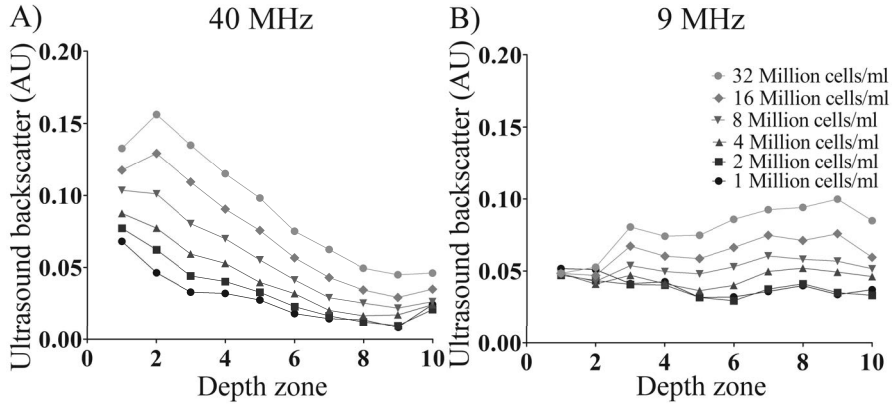

Figure 6.2: Depth-dependent ultrasound backscatter (arbitrary units (AU)) at 40 MHz (A) and at 9 MHz (B) for different cell number densities. Increase in the zone 10 at 40-MHz is due the specular reflection from scaffold-container interface. In the analyses, constant thickness of the scaffolds (3.9 mm) was divided into 10 equally thick depth zones.

In study **III**, the dependence of the ultrasound backscatter on CND was evaluated numerically (Figure 6.3). A similar increasing trend was observed as found in the experimental results reported in study **I** (Figure 6.3). This was also observed in study **IV**, where the increase in the CND in the randomly distributed cell models elevated the amplitude of the spectra (Figure 6.4). In addition, a strong correlation was observed between cell spacing and *AIB* (R^2 = 0.94, data not shown). However, the increase in CND did not affect the apparent frequency dependence of backscatter (*AFB*). The increase in the cell size had only a minor effect on *AIB* for cells larger than 8 µm, while *AFB* continuously decreased from 0.15 dB/MHz to −0.25 dB/MHz for cell sizes from 8 µm to 16 µm and increased again to −0.15 dB/MHz with the largest simulated cell size 20 µm (data not shown).

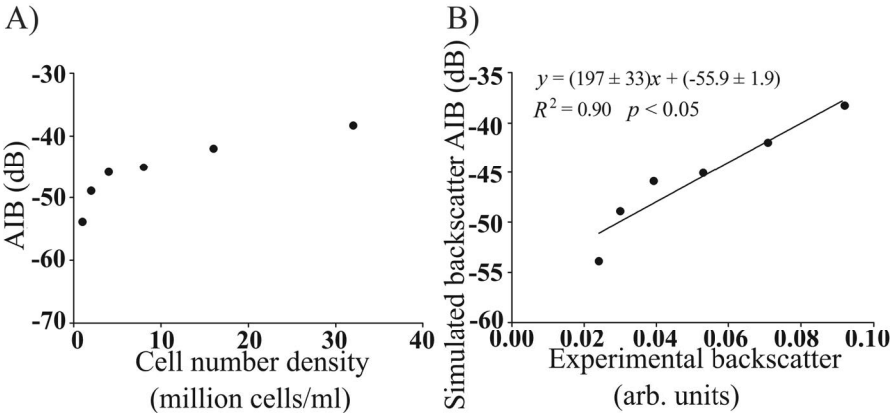

Figure 6.3: A) Simulated 40-MHz ultrasound backscatter for different cell number densities. B) Experimental (study **I**) and simulated (study **III**) backscatter values showed a strong correlation.

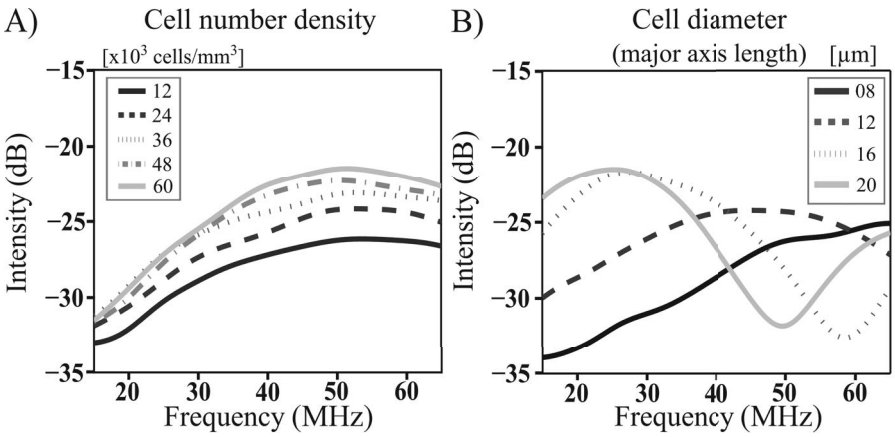

Figure 6.4: (A) Increasing cell number density results in an frequency independent amplitude increase while (B) increasing cell size with fixed cell number density changes the amplitude and frequency dependence of backscatter.

6.1.2 Effect of cell spacing in superficial zone cartilage on ultrasound backscatter

In study **IV**, characteristic frequency peaks in depth-dependent frequency spectra (DFS) were observed in the FDTD simulations with organized cell layers in the superficial zone (Figure 6.5). When three or more aligned cell layers (N_c) were present, a peak was detected in DFS (Figure 6.5B). The peak amplitude increased and had a narrower width when the number of cell layers (N_c) increased. When N_c was more than 5, no further effects were observed in DFS. When the randomness in the depth-wise position of cells within the layer (V_c) was increased, peak amplitude decreased and peak width increased (Figure 6.5A). When V_c was increased, the peak amplitude decreased or even disappeared *e.g.* with 20 µm spacing the peak vanished when V_c was 8 µm.

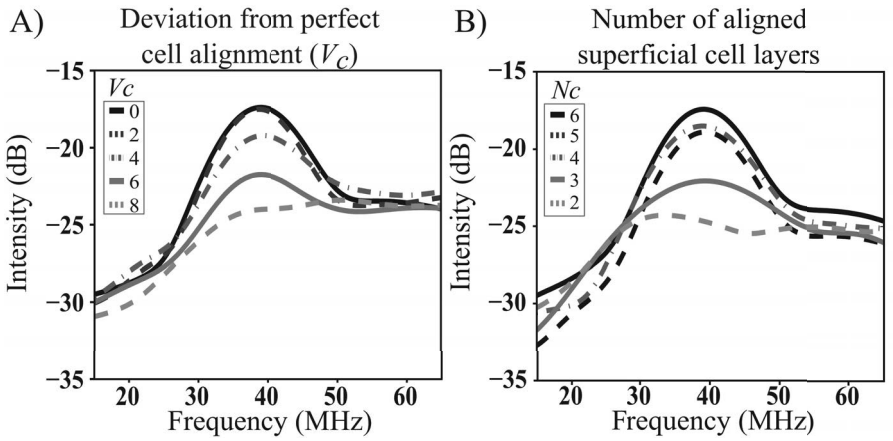

Figure 6.5: A) Variation in location (V_c) and B) number of cell layers (N_c) affected the shape of the scattering spectrum. Regular chondrocyte spacing was set to (S_c = 20 µm) in the superficial zone.

The peak position in DFS was shifted when the spacing between cell layers (S_c) increased (Figure 6.6). Moreover, the second peak occurred at 53.75 MHz $\pm$ 0.29 MHz, for example when S_c was 30 µm (Figure 6.6). For the models having spacings of 15 µm, 20 µm, 25 µm, 30 µm, 35 µm, and 40 µm the corresponding spacings estimated based on DFS were 15.1 $\pm$ 0.15 µm, 20.4 $\pm$ 0.18 µm, 26.4 $\pm$ 0.36 µm, 29.8 $\pm$ 0.12 µm, 35.43 $\pm$ 0.40 µm, and 40.9 $\pm$ 0.13 µm. The average absolute error in cell spacing estimated based on DFS was 0.2 $\pm$ 0.1 µm. The spacing algorithm failed in 97% and of the simulations which there was a randomized structure but only in 1% of the simulations with a layered structure. No dependencies were found between CND and *AIB* or *AFB* (data now shown).

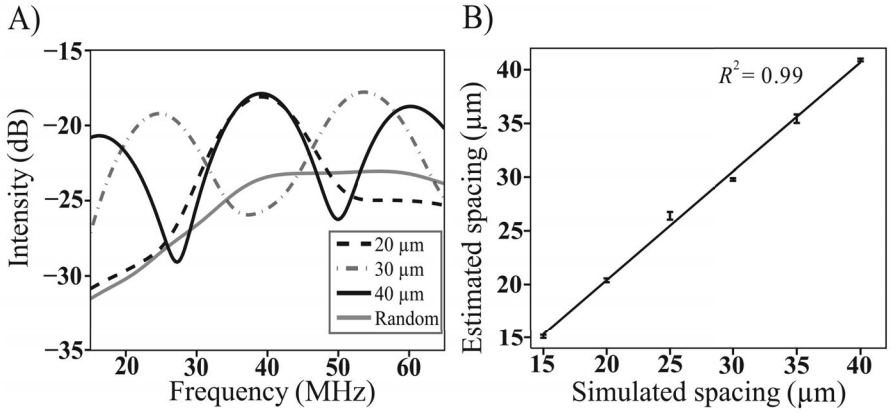

Figure 6.6: A) Log-compressed difference spectra evaluated at different cell spacings. B) Linear correlation of estimated and simulated chondrocyte spacing. Standard deviations are marked with the error bars.

Estimation of chondrocyte spacing with 50-MHz ultrasound

It was demonstrated that the quantitative ultrasound (QUS) measured cell spacing between 100 µm and 250 µm depths was significantly lower ($p < 0.001$) in the Mankin score $\leq$ 3 group when compared with Mankin score groups 5 and 6 (Table 6.1). However, this was not observed in light microscopy (LM). In all samples, moderate to strong ($p < 0.05$) positive correlations between QUS measured cell spacing and cartilage-depth were observed (average R^2 = 0.55 and QUS spacing vs. depth slope = 0.03 µm/µm, Table 6.1).

A comparison between QUS and LM based cell spacing estimation revealed that QUS based spacing estimates were significantly higher than those based on LM ($p < 0.01$). This was especially pronounced in those samples with Mankin score of 5 or 6 ($p < 0.001$, χ^2 = 42.9) in comparison with samples with lower a Mankin score *i.e.*, 1 or 3 ($p < 0.05$, χ^2 = 6.1). Moreover, for samples with a low Mankin score ($\leq$ 3), a statistically significant clear correlation (R^2 = 0.59, $p < 0.001$) between LM and QUS spacing estimates was found when six average spacing values per sample between depths of 100 µm and 250 µm were compared (Figure 6.7A). However, with higher Mankin scores (*i.e.*, $\geq$ 5) no significant correlation was found (R^2 = 0.0007, n.s.). When all samples were pooled, the correlation was statistically significant but weak (R^2 = 0.13, $p < 0.05$).

Conventional backscatter parameters *AIB* and *AFB* were found to be significantly ($p < 0.05$) different between different Mankin score groups *i.e.* between ≤ 3 vs. 5 and ≤ 3 vs. 6 (Table 6.1). Strong or moderate correlations between *AFB* (Figure 6.7B) or *AIB* ($R^2 = 0.59$, $p \leq 0.0001$) and QUS based spacing values were observed.

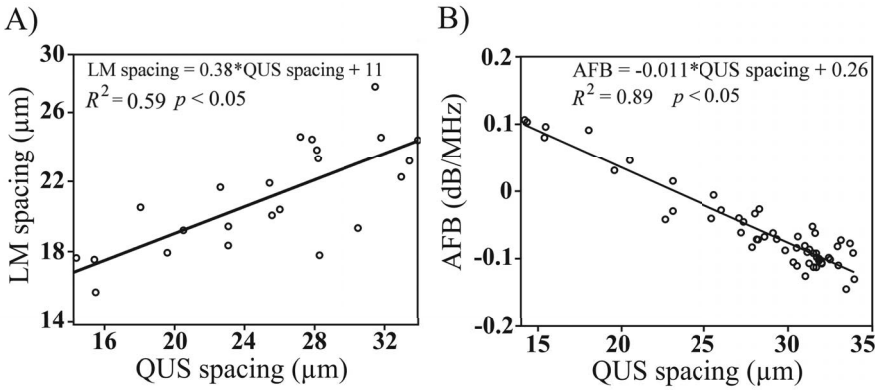

Figure 6.7: A) Linear correlation of LM and QUS based chondrocyte spacing values in the low Mankin score (≤ 3) samples ($n = 4$). B) Linear correlation between AFB and QUS based spacing values in all samples ($n = 9$). Values were determined between depths of 100 µm and 250 µm with 25 µm interval. This yielded 6 values per sample.

Table 6.1: Quantitative ultrasound (QUS) and light microscopy (LM) based chondrocyte spacing estimates (mean ± SD of spacing values determined between the depths of 100 µm and 250 µm) presented for all samples. Slope values of linear fits for spacing versus depth and the corresponding significant ($p \leq 0.05$) R^2 values are presented.

Sample	LM spacing (µm)	QUS spacing (µm)	*AIB* (dB)	*AFB* (dB/MHz)	LM spacing/depth	R^2 spacing vs. depth	QUS spacing/depth	R^2 spacing vs. depth	Mankin score
1	20.0 ± 1.2	22.6 ± 3.0	-28.8 ± 3.0	0.016 ± 0.05	–	n.s.	0.07	0.50	1
2	17.4 ± 1.4	17.0 ± 3.5	-25.4 ± 2.3	0.05 ± 0.06	0.02	0.48	0.06	0.50	3
3	$21.9 \pm 2.8*$	31.8 ± 2.1	-30.5 ± 3.8	-0.10 ± 0.05	0.02	0.35	0.04	0.71	3
4	$24.3 \pm 1.8*$	28.1 ± 2.0	-33.1 ± 3.4	-0.07 ± 0.02	–	n.s.	0.04	0.69	3
5	$22.1 \pm 0.7*$	28.2 ± 0.9	-34.4 ± 3.1	-0.05 ± 0.002	–	n.s.	0.01	0.52	5
6	$21.0 \pm 3.2*$	32.8 ± 1.0	-33.0 ± 2.4	-0.07 ± 0.002	–	n.s.	0.02	0.49	5
7	$21.7 \pm 1.1*$	32.0 ± 0.5	-31.7 ± 2.1	-0.09 ± 0.01	−0.02	0.34	0.01	0.29	6
8	$21.1 \pm 5.6*$	31.3 ± 0.5	-31.8 ± 1.1	-0.09 ± 0.02	0.1	0.68	0.01	0.62	6
9	$17.4 \pm 1.5*$	30.8 ± 0.7	-33.1 ± 3.9	-0.11 ± 0.02	–	n.s.	0.01	0.66	6

* spacing values determined with LM and QUS are significantly different ($p < 0.05$). n.s. denotes not significant.

6.2 ULTRASOUND BACKSCATTER FROM COLLAGEN

6.2.1 Effect of collagen concentration on ultrasound backscatter

In study **I**, ultrasound backscatter increased significantly with both frequencies ($p < 0.05$) when the collagen concentrations increased in the scaffolds (Figure 6.8). However, the backscattering of the 9-MHz ultrasound was not as sensitive as that of 40-MHz ultrasound to the variations in collagen concentration. Moreover, with 40-MHz ultrasound, the skewness of the intensity distribution also significantly ($p < 0.05$) differed between the different collagen concentrations. However, this was not observed with 9-MHz ultrasound.

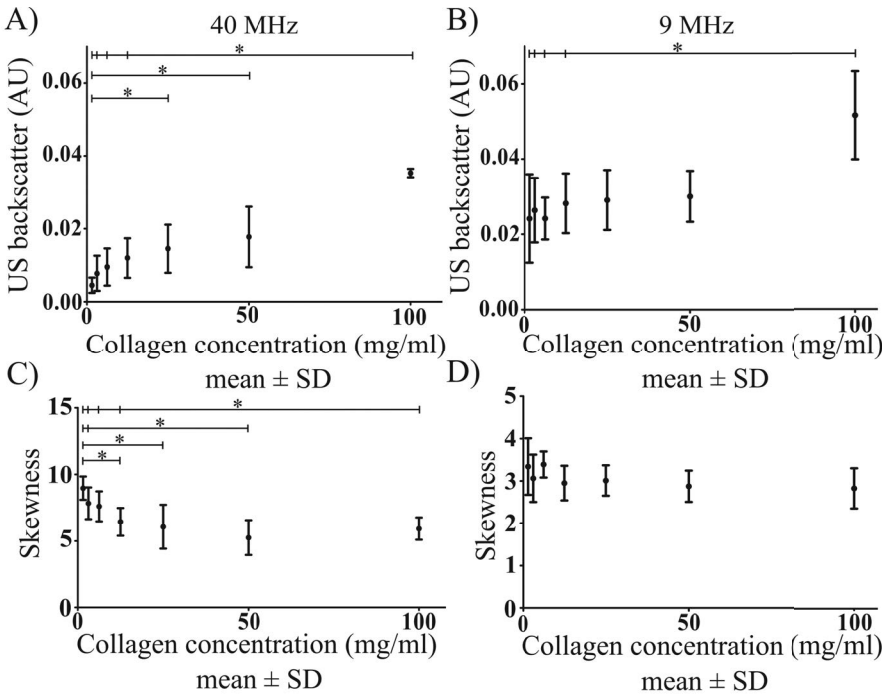

Figure 6.8: 40-MHz (A) and 9-MHz (A) ultrasound backscatter (arbitrary units, (AU)) as a function of collagen concentration. For 40-MHz (C) and 9-MHz (D) skewness of the intensity distribution as a function of collagen concentration. Standard deviations are marked with error bars. *$p < 0.05$.

With 40-MHz ultrasound at higher collagen concentrations ($\leq$ 12.5 mg/mL), a decrease in the backscattering as a function of depth was detected (figure 6.9) but with 9 MHz, no similar depth dependence was observed.

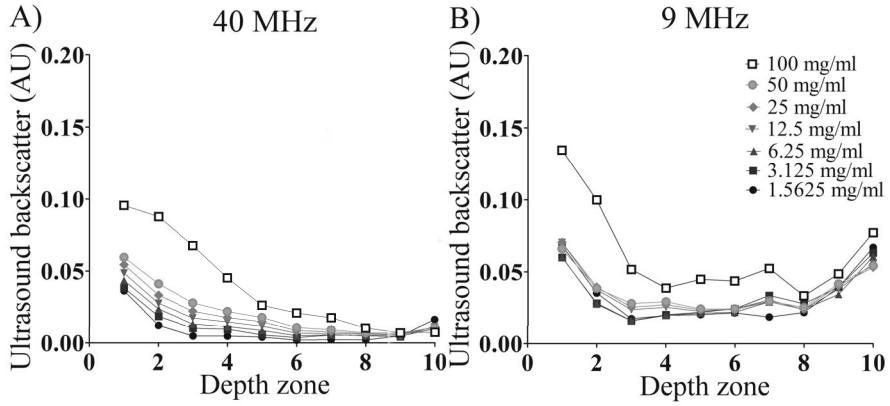

Figure 6.9: Depth-dependent ultrasound backscatter at 40 MHz (A) and at 9 MHz (B) (arbitrary units (AU)) for different collagen concentrations. In the depth zones 9–10 at 9-MHz ultrasound, elevation in the backscatter is caused by the reflection and scattering from subchondral bone.

In study **III**, the dependence of the ultrasound backscatter on the collagen concentration was numerically evaluated using FDTD modelling (Figure 6.10). A similar increasing trend was observed in the *AIB* as found in the experiments conducted in study **I**.

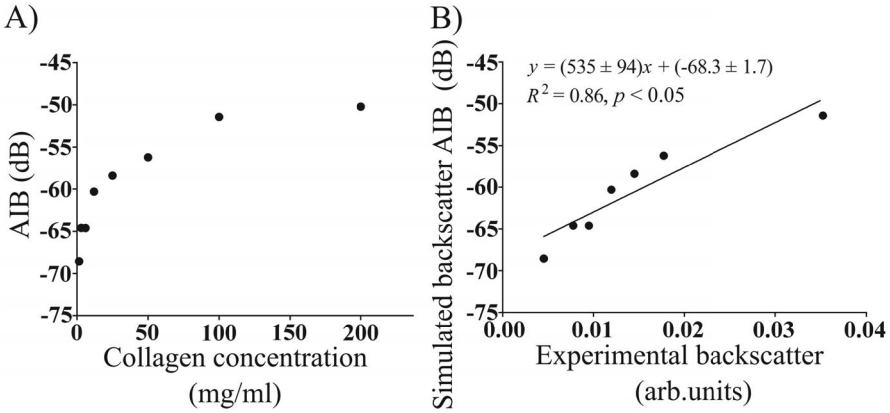

Figure 6.10: A) Simulated apparent integrated backscatter (*AIB*) as a function of collagen concentration. B) Linear fit between experimental (study **I**) and simulated (study **III**) backscatter values.

6.2.2 Anisotropy of ultrasound backscatter

In study **II**, *AIB* and backscattering determined from the ultrasound images were significantly higher in the transitional and deep zones when the measurements were conducted through the lateral (cut) surface instead of through the articular surface (Figure 6.11 and Table 6.2).

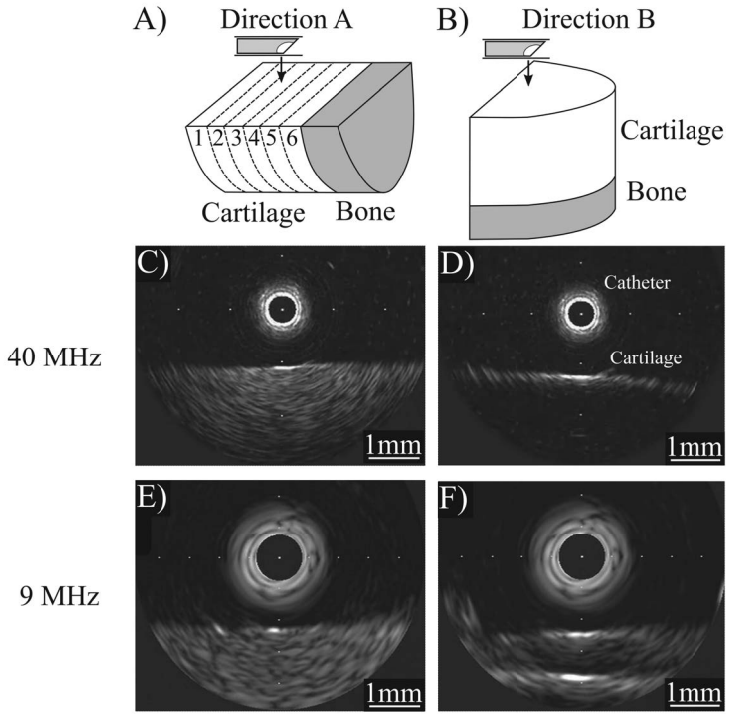

Figure 6.11: A) In direction A ultrasound wave incidence is parallel to the articular surface (lateral side A, C, E). The lateral side was divided into six sections from surface to cartilage-bone interface (A), and each section was independently imaged and measured. In direction B ultrasound incidence is perpendicular to the articular surface (B, D, F). 40-MHz (C, D) and 9-MHz (E, F) ultrasound images through lateral (cut) surface (C, E) and through articular surface (D, F).

Table 6.2: Ultrasound backscatter values measured through lateral (cut) surface and articular surface†.

	Orientation	*AIB* (dB)	Backscatter (AU)
40 MHz	Lateral (cut) surface		
	1	-63.0 ± 4.2*	0.044 ± 0.014
	2	-63.5 ± 3.2*	0.059 ± 0.018*
	3	-62.0 ± 5.0*	0.078 ± 0.033*
	4	-60.8 ± 6.1	0.100 ± 0.042*
	5	-58.2 ± 6.4	0.114 ± 0.048*
	6	-53.8 ± 5.6*	0.129 ± 0.052
	Articular surface	-60.0 ± 3.7	0.036 ± 0.011
9 MHz	Lateral (cut) surface		
	1	-59.1 ± 6.1*	0.19 ± 0.05*
	2	-53.6 ± 6.0*	0.26 ± 0.03
	3	-51.1 ± 6.5	0.30 ± 0.04
	4	-47.1 ± 4.2	0.35 ± 0.05*
	5	-46.6 ± 5.1	0.39 ± 0.05*
	6	-43.3 ± 4.3*	0.43 ± 0.04*
	Articular surface	-48.5 ± 5.4	0.28 ± 0.06

AIB = apparent integrated backscatter.
† Numbers 1–6 refer to six sections from the cartilage surface to the cartilage-bone interface in the lateral (cut) side. Backscatter was measured from the ultrasound B-mode images and was significantly higher when measured through the lateral cut surface in middle and deep cartilage sections.
*$p < 0.05$ Wilcoxon signed rank test comparison of backscatter measured through articular surface and lateral (cut) surface.

Depth-dependent ultrasound backscattering measured from ultrasound B-mode videos is illustrated in figure 6.12. The decrease in the rate of the backscatter measured through the articular surface was higher than that of backscatter measured through the lateral (cut) surface.

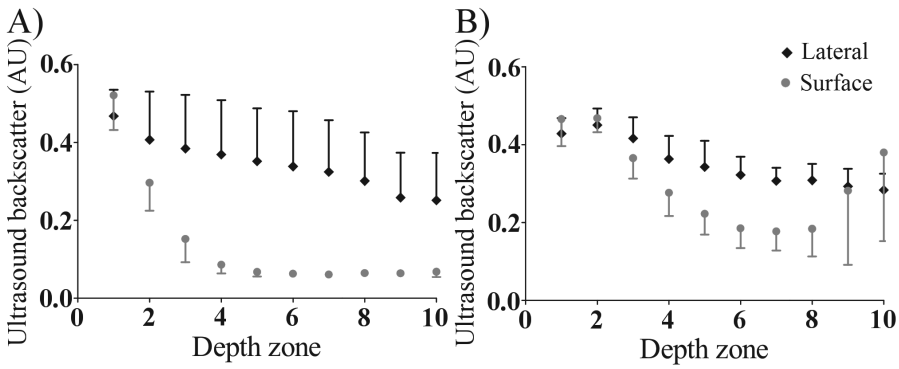

Figure 6.12: Depth-dependent ultrasound backscatter profiles in arbitrary units (AU) (mean ± SD) measured thought the middle part (section 4) of the lateral (cut) surface (black) and through the articular surface (gray) at 40 MHz (a) and at 9 MHz (b).

In the lateral direction, the correlation (ρ) between collagen orientation (angle with respect to the articular surface) and ultrasound (9 MHz and 40 MHz) backscatter ranged from 0.33 to 0.61 ($p \leq 0.01$), and the correlation between collagen concentration and ultrasound backscattering ranged from 0.43 to 0.59 ($p \leq 0.01$).

For approximately 80% of the cartilage thickness, the collagen fiber orientation was perpendicular to the articular surface and the PG concentration rapidly increased from the surface to the transitional zone (Figure 6.13). Moreover, the relative chondron area was 7 $\pm$ 3%, and the size of the individual chondrons increased towards the cartilage-bone interface.

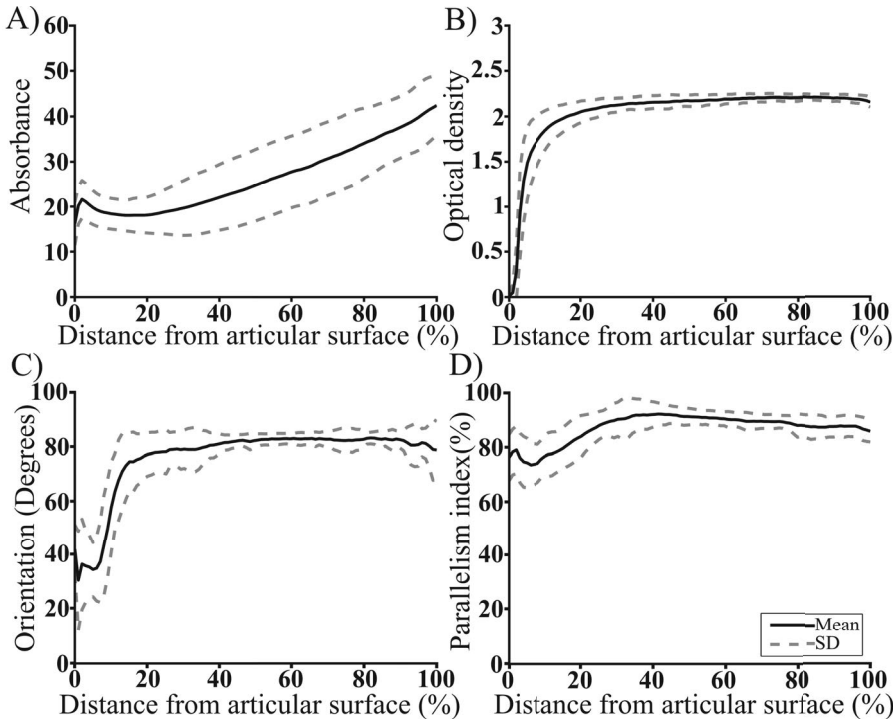

Figure 6.13: Depth profiles (mean $\pm$ SD) of (A) relative collagen concentration determined as integrated absorbance in arbitrary units in the amide I region with Fourier transform spectroscopy, (B) relative proteoglycan distribution determined as optical density, (C) collagen orientation and (D) parallelism index determined with polarized light microscopy.

In study **III**, the effect of collagen fibril orientation on ultrasound backscatter was investigated by generating two models with collagen fibril orientations either perpendicular to or in parallel with the ultrasound wave propagation direction. The value of *AIB* was highest in the model where the orientation of collagen fibrils was perpendicular to the wave propagation direction (table 6.3).

Table 6.3: Speed of sound (SOS) and apparent integrated backscattering (*AIB*) of collagen models with fibrils oriented in parallel, perpendicular to randomly with the ultrasound propagation direction. Collagen concentration in all the models was 100 mg/mL.

Orientation of fibrils	*SOS* (m/s)	*AIB* (dB)
Parallel	1457.4	−68.1
Perpendicular	1454.6	−19.1
Random	1455.7	−51.4

6.3 ELASTO-ACOUSTIC PROPERTIES OF CARTILAGE AND CHONDROCYTES OBTAINED FROM HIGH RESOLUTION SAM

In study **IV**, a 250-MHz SAM could distinguish between the extracellular matrix and chondrocytes (figure 6.14). The corresponding mechanical and acoustical properties of chondrocytes and surrounding extracellular matrix are presented in table (6.4).

Table 6.4: Mean and standard deviations of the mechanical and acoustical properties of extracellular matrix and chondrocytes determined with a 250-MHz SAM.

Material	Z (MRayl)	*SOS* (m/s)	ρ (g/cm^3)	K (GPa)
Extracellular matrix	1.75 ± 0.03	1590 ± 20	1.10 ± 0.01	2.80 ± 0.07
Chondrocytes	1.64 ± 0.01	1568 ± 8	1.04 ± 0.012	2.56 ± 0.01

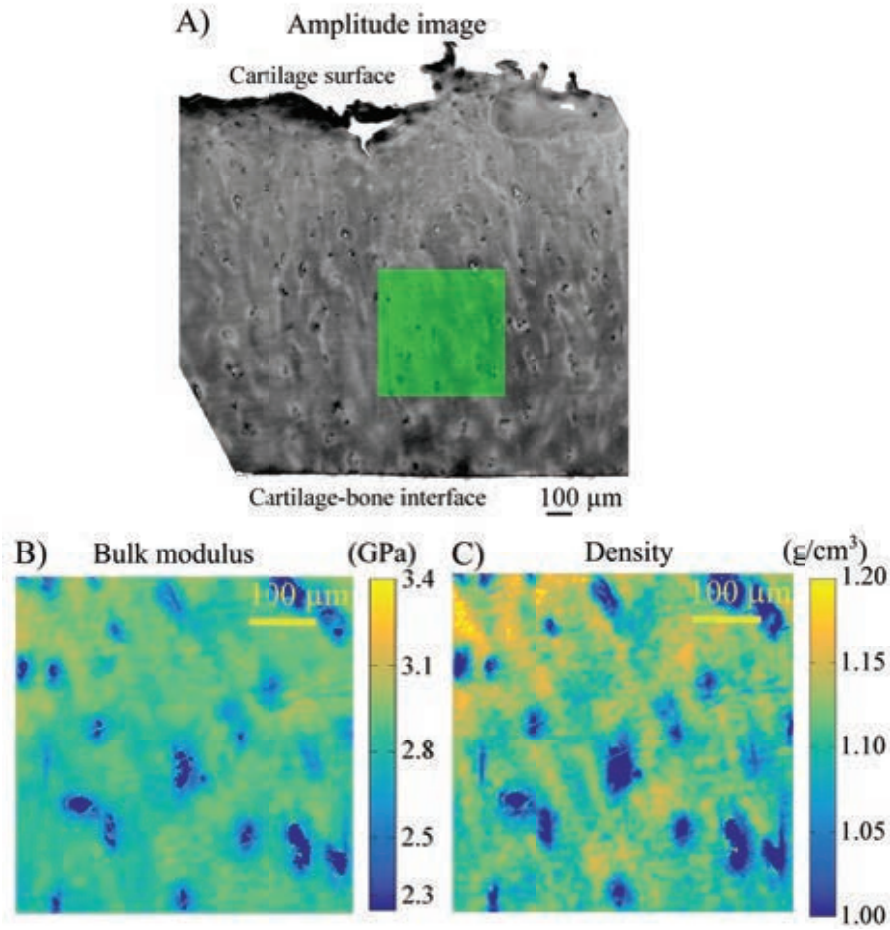

Figure 6.14: A) Scanning acoustic microscopy amplitude image of a human articular cartilage section. The region of interest where average values for Z, c, ρ, and K were determined is highlighted in green. Corresponding bulk modulus and density maps are presented in B) and C), respectively.

7 Discussion

Osteoarthritic changes in cartilage tissue composition and structure can be detected with quantitative ultrasound techniques, and the analysis of the ultrasound backscatter enables the characterization of the subsurface properties of cartilage [29,34,87,125,139]. However, it is still unclear how the constituents of cartilage affect ultrasound backscattering. The aim of this thesis was to brigde this gap in knowledge by studying experimentally and numerically the effect of chondrocytes and collagen on the ultrasound backscatter.

In studies **I** and **II**, the effects of articular cartilage composition and structure on the ultrasound backscatter were investigated experimentally. In study **III**, the benefits of FDTD modelling in the simulation of ultrasound backscatter arising from collagen and chondrocytes were evaluated by constructing FDTD models with geometries mimicking the experimental set up applied in study **I**. In study **IV**, two scanning acoustic microscopes were used to quantify the acoustic properties of articular cartilage. High resolution 250-MHz scanning acoustic microscopy of thin cartilage sections was used to determine material parameters for chondrocytes and extracellular matrix needed in the FDTD modelling. 50-MHz SAM was used to obtain backscatter data from unprocessed human cartilage samples. Finally, the possibility to estimate the cell spacing from the ultrasound spectrum was studied numerically first with FDTD simulations and then experimentally.

7.1 ULTRASOUND BACKSCATTER FROM CHONDROCYTES

Effect of cell number density on ultrasound backscatter

Several studies have investigated ultrasound backscattering arising from different cells [166–168]. In these studies, the effect of the cell structure, *e.g.* the change of cell morphology during apoptosis, on the ultrasound backscatter has been investigated by calculating spectral parameters and the ultrasound backscattering coefficient. Despite the extensive research on ultrasound imaging of articular cartilage, the specific contribution of the number density of chondrocytes to the ultrasound backscatter has not been investigated experimentally. In study **I**, ultrasound backscatter was found to increase with increasing cell number density. The findings of the study **I** are in line with a more recent report where a significant correlation was found between cell number density and ultrasound backscatter amplitude in articular cartilage [87]. Furthermore in the recent study of Männicke *et al.* 2016, the value of the AIB parameter was found to be positively correlated (R^2 = 0.51) with the combination of cell number density and collagen concentration in a model in which collagen orientation was approximately perpendicular (>70°) to the ultrasound propagation direction [139].

In study **III**, FDTD simulations revealed an increase in AIB as the cell number density increased. This result is similar to the experimental finding in study **I**. An increase in the backscatter spectrum amplitude as a function of cell number density was also observed in the simulations conducted in study **IV**. While these 2D FDTD-models provided a good insights into how the cell number density and

the size of the cells affect ultrasound backscatter, more realistic models with more physiological cell geometries in 3D *e.g.* obtained by means of confocal microscopy should be investigated in future. This would add important knowledge on the effect of biological variation in the size and shape of chondrocytes on the ultrasound backscatter.

Effect of chondrocyte arrangement on ultrasound backscatter

The organization of chondrocytes varies in the different cartilage zones [43,61]. In the superficial zone, cells are isolated and smaller than those in the deep zone. Moreover, the cell number density is higher in the superficial zone and shape of the cells in the superficial zone is ellipsoidal. In the deep zone, the cells are more round and can form columns [169]. In study **IV**, the arrangement of cells into layers in the superficial zone was found to cause a coherent peak in the depth dependent frequency spectrum of the backscatter in both simulations and experiments. By analysing the peak position, a depth-dependent estimate for average cell spacing in the superficial zone could be determined.

If the scatteres are separated by a constant distance ($\Delta t c_0$) in the direction of the incident wave, then the oscillatory coherent part will add up at a frequency $1/\Delta t$ which can be observed as a peak in the power spectrum. This was verified in the simulations where a detectable peak appeared at the expected frequency. However, the scatterers, *i.e.* cells in articular cartilage, are embedded in the extracellular matrix which affects the observed backscatter spectrum [139]. This property, as well as multiple scattering, will introduce non-linearity into the backscatter power spectrum. Moreover, the architecture of the collagen network can influence the shape and orientation of chondrocytes [169], and therefore the structural patterns of superficial chondrocytes may be related to the structure of the collagen network in that area [60]. Nevertheless, the spacings estimated from the backscatter spectrum and those based on light microscopy were strongly correlated, supporting the idea that the resonance peak detected in the superficial zone was related to cell spacing.

In early OA, the articular surface degenerates, triggering degradation of the collagen network and depletion of proteoglycans. These changes increase the water content of cartilage causing cartilage swelling. Structural changes affect the overall cell distribution within the tissue, and moreover in OA, chondrocytes proliferate and form cell clusters [170,171]. Changes in cell distribution were observed in study **IV** where the average cell spacing estimated from the backscatter spectrum was found to be significantly higher in more degenerated cartilage (Mankin ≤ 3 vs. Mankin ≥ 5).

Ultrasound backscatter in cartilage is commonly quantified using *AIB* and *AFB* parameters [34,87]. When combined, these parameters are potentially good indicators for early OA [172], since frequency dependence of ultrasound backscatter can be quantified using *AFB*, whereas *AIB* assesses the magnitude of the power spectrum. In study **IV**, when examined speciments with increasing Mankin scores, *AIB* decreased and *AFB* changed from being positive to negative. Moreover, correlations were found between cell spacing and *AIB* and *AFB* parameters. If these parameters are determined alone while neglecting possible coherent scattering due to cell spacing, this might lead to erroneous conclusions and weaken the predictive power of QUS-based OA diagnostic tools. Future studies should aim at separating the incoherent and coherent scatter information in order to enable determine of QUS parameters that are related to cell morphology. This could be accomplished by adapting other signal processing approaches such as cepstral analysis [173].

7.2 ULTRASOUND BACKSCATTER FROM COLLAGEN

Effect of collagen concentration on ultrasound backscatter

In study **I**, ultrasound backscattering increased in parallel with an increase in the collagen concentration, with 40-MHz ultrasound being more sensitive than 9-MHz ultrasound in detecting this change. This may be related to the shorter wavelength of 40-MHz ultrasound which is more sensitive at detecting smaller structures such as collagen fibrils [174].

In study **I**, collagen was dissolved in hydrochloric acid and therefore was not arranged in an organized network. Furthermore, the typical concentration of the collagen in human cartilage is around 200 mg/mL, which is more than the maximum collagen concentration used in study **I** [155]. However, due to difficulties in dissolving high collagen concentration in HCl, it was not possible to generate higher collagen concentrations in agarose scaffolds. In a previous study, collagen was proposed as being the main scatterer of ultrasound in articular cartilage [125]. Surprisingly, the backscatter measured from collagen was lower than that from chondrocytes. This was also observed in the simulations conducted in study **III**. In the future, more realistic FDTD-models combining both chondrocytes and the collagen network should be created to study the combined effects of collagen and chondrocytes on ultrasound backscatter in 3D.

7.3 ANISOTROPY OF ULTRASOUND BACKSCATTER

Ultrasound backscattering has been found to be anisotropic in tissues having a highly organized collagen network, such as myocardium and tendons [175]. In study **II**, ultrasound backscatter was higher when measured in a direction parallel to the articular surface *i.e.* through the lateral (cut) side of the cartilage. In this setup, the direction of the ultrasound propagation was perpendicular to the collagen orientation in deep cartilage.

In the superficial zone the collagen fibers are oriented in parallel with the articular surface, in the transitional zone, they are randomly oriented and finally in the deep zone, they are perpendicular to the articular surface. The ultrasound was found to scatter more when it was propagating in a direction perpendicular with the collagen fiber orientation. This was observed also in the simulations conducted in study **III**. Moreover, in the repair tissue where collagen network is unorganized ultrasound backscatter has been found to be significantly higher when compared to that in healthy cartilage [125, 176]. The findings in studies **II** and **III** are supported by Männicke *et al.* 2016, where a positive correlation was found between the collagen concentration and *AIB*, when collagen orientation was perpendicular (>70°) in the ultrasound propagation direction [139].

In study **II**, 9-MHz and 40-MHz ultrasound transducers suitable for arthroscopic use were exploited [26, 29, 107]. The 9-MHz ultrasound enables full-depth cartilage imaging and an evaluation of subchondral bone [29]. The 40-MHz ultrasound provides high-resolution ultrasound images and can detect changes in the articular surface. However, OA related changes in the deep cartilage cannot be visualized in a 40-MHz ultrasound image due to attenuation, especially in thick human cartilage. *AIB* values were systematically higher when determined with 9-MHz ultrasound compared with those determined with 40-MHz ultrasound. Moreover, *AIB* values

which were measured through the articular surface were in the same range as those reported previously for 40-MHz [28] and 9-MHz ultrasound [29].

The following limitations of the study **II** should be mentioned. Cutting of cartilage modifies the integrity of the tissue structure and may cause swelling. We attempted to minimize this problem by keeping the cartilage attached to the subchondral bone. Indeed, polarized light microscopy images of lateral cartilage sections revealed that the collagen orientation in cartilage was normal and consistent with the literature [177].

When backscatter was evaluated from the B-mode video images at 9-MHz through the articular surface, a high variation was observed in the depth zones 9 and 10. This might have been due to reflection and scatter from calcified cartilage and subchondral bone. This is possible, since the depth zones in the analysis window were based on the thickness measured with OCT and sound speed values obtained from Patil *et al.* 2004 [130]. Therefore, when the backscatter was determined from the whole cartilage thickness, zones 1 and 10 were removed from the analyses. With 40-MHz ultrasound, this variability was not observed in the zones 9 and 10, since the ultrasound wave had become attenuated before it reached the cartilage-bone interface. Statistically significant differences were observed when backscatter magnitude (from B-mode images) was measured through the articular surface and through the middle lateral (cut) surface (sections 4 and 5). However, with *AIB*, the limit for statistical significance could not be reached. The reason for this is the averaged B-mode image which consists of more signal data from multiple frames compared to that of *AIB*, which is being calculated from only a single ultrasound signal.

7.4 ELASTO-ACOUSTIC PROPERTIES OF CHONDROCYTES AND EXTRACELLULAR MATRIX

In study **IV**, 250-MHz SAM enabled the quantification of the elasto-acoustic parameters for chondrocytes and extracellular matrix of fixed cartilage sections. This is the first study to estimate bulk modulus or acoustic impedance values for chondrocytes using SAM.

The material properties derived from the fixed cartilage sections should be carefully considered, since the embedding, de-paraffinization and rehydration of the samples can alter the mechanical properties of tissues [178]. Moreover, the chondrocytes might have been damaged during the cutting of tissue sections. Nonetheless, the value of the speed of sound obtained for extracellular matrix is in agreement that obtained in a previous *in vivo* study [179]. Furthermore, the cartilage-to-water acoustic impedance ratio reported in study **IV** (1.8 MRayl/1.5 MRayl = 1.2) is in line with that provided in the previous study of Tepic *et al.* 1983 (1.1–1.2) [180].

In this study, only the central part of the vertical cartilage section was analyzed due to problems with the detachment of the specimen from the glass slide. In the future, this problem could be resolved by using a more dense coupling medium (*e.g.* ultrasonic gel) between the transducer and the tissue section. However, it is possible that the ultrasonic gel would attenuate and distort the high frequency ultrasound wave more than water and this would need to be taken into account in the analyses. The elasto-acoustic properties were determined from vertical cartilage sections and the high frequency ultrasound wave propagated parallel to the cartilage surface. In the FDTD-simulations, the elastic properties were assumed to be isotropic and

the ultrasound wave was propagated in the direction perpendicular to the articular surface. However, this assumption may not be valid and should be investigated more carefully in the future by preparing horizontal tissue sections from varying tissue depths, *i.e.* from the superficial to the deep zone.

In the future, by using cryo-sectioned cartilage sections, limitations related to fixation and cell cutting could be avoided. Moreover, by using a higher frequency acoustic microscope *e.g.* a 500-MHz SAM, the lateral resolution of the quantitative elasto-acoustic maps could be enhanced [161].

8 Summary and conclusions

In this thesis, ultrasound backscatter from articular cartilage samples and collagen or chondrocytes in agarose scaffolds was investigated by applying both experimental and numerical methods. The suitability of numerical modelling to simulate ultrasound propagation and scattering was tested by generating simulation geometries mimicking the experimental setups used in the initial studies in this thesis. The anisotropy of ultrasound (9 MHz and 40 MHz) backscatter was investigated in bovine articular cartilage samples. Finally, the feasibility of ultrasound backscatter to estimate cell spacing in superficial zone cartilage was numerically and experimentally evaluated.

The following conclusions can be drawn based on the findings emerging from this thesis:

1. Both collagen and chondrocytes contribute to the ultrasound backscattering when they are embedded in agarose.
2. Ultrasound backscatter is anisotropic in cartilage and the backscatter is highest when the orientation of collagen fibers is perpendicular with ultrasound propagation direction.
3. FDTD modelling was suitable for simulating ultrasound wave propagation and scattering in agarose scaffolds containing different concentrations of collagen and chondrocytes.
4. High frequency (250-MHz) scanning microscopy revealed different elasto-acoustic properties for chondrocytes and the extracellular matrix.
5. Cell spacing in superficial zone was found to be related to coherent ultrasound backscatter and furthermore, the conventional ultrasound parameters (*AIB* and *AFB*) were observed to be correlated with cell spacing.

BIBLIOGRAPHY

[1] R. C. Lawrence, "Estimates of the prevalence of arthritis and other rheumatic conditions in the United States. Part II," *Arthritis and Rheumatism* **58**, 26 (2008).

[2] V. L. Johnson and D. J. Hunter, "The epidemiology of osteoarthritis," *Best Practice & Research Clinical Rheumatology* **28**, 5–15 (2014).

[3] T. Neogi and Y. Zhang, "Epidemiology of osteoarthritis," *Rheumatic Diseases Clinics of North America* **39**, 1–19 (2013).

[4] J. A. Buckwalter and J. A. Martin, "Osteoarthritis," *Advanced Drug Delivery Reviews* **58**, 150–167 (2006).

[5] E. Yelin, L. Murphy, M. G. Cisternas, A. J. Foreman, D. J. Pasta, and C. G. Helmick, "Medical care expenditures and earnings losses among persons with arthritis and other rheumatic conditions in 2003, and comparisons with 1997," *Arthritis and Rheumatism* **56**, 1397–1407 (2007).

[6] R. Bitton, "The economic burden of osteoarthritis," *The American Journal of Managed Care* **15**, S230–235 (2009).

[7] M. Heliövaara, P. Slätis, and P. Paavolainen, "Nivelrikon esiintyvyys ja kustannukset," *Duodecim* **124**, 1869–1874 (2008).

[8] B. Sharif, J. Kopec, N. Bansback, M. M. Rahman, W. M. Flanagan, H. Wong, P. Fines, and A. Anis, "Projecting the direct cost burden of osteoarthritis in Canada using a microsimulation model," *Osteoarthritis and Cartilage* **23**, 1654–1663 (2015).

[9] A. J. Carr, "Beyond disability: measuring the social and personal consequences of osteoarthritis," *Osteoarthritis and Cartilage* **7**, 230–238 (1999).

[10] J. Bookwala, T. L. Harralson, and P. A. Parmelee, "Effects of pain on functioning and well-being in older adults with osteoarthritis of the knee," *Psychology and Aging* **18**, 844–850 (2003).

[11] H. Madry, F. P. Luyten, and A. Facchini, "Biological aspects of early osteoarthritis," *Knee surgery, Sports traumatology, Arthroscopy* **20**, 407–422 (2012).

[12] K. Chiba, M. Ito, M. Osaki, M. Uetani, and H. Shindo, "In vivo structural analysis of subchondral trabecular bone in osteoarthritis of the hip using multi-detector row CT," *Osteoarthritis and Cartilage* **19**, 180–185 (2011).

[13] M. B. Goldring, "The role of the chondrocyte in osteoarthritis," *Arthritis and Rheumatism* **43**, 1916–1926 (2000).

[14] M. B. Goldring, "Chondrogenesis, chondrocyte differentiation, and articular cartilage metabolism in health and osteoarthritis," *Therapeutic Advances in Musculoskeletal Disease* **4**, 269–285 (2012).

[15] P. M. Van der Kraan and W. B. Van den Berg, "Chondrocyte hypertrophy and osteoarthritis: Role in initiation and progression of cartilage degeneration?," *Osteoarthritis and Cartilage* **20**, 223–232 (2012).

[16] K. M. Jordan, N. K. Arden, M. Doherty, B. Bannwarth, J. W. Bijlsma, P. Dieppe, K. Gunther, H. Hauselmann, G. Herrero-Beaumont, P. Kaklamanis, S. Lohmander, B. Leeb, M. Lequesne, B. Mazieres, E. Martin-Mola, K. Pavelka, A. Pendleton, L. Punzi, U. Serni, B. Swoboda, G. Verbruggen, I. Zimmerman-Gorska, and M. Dougados, "EULAR Recommendations 2003: an evidence based approach to the management of knee osteoarthritis: Report of a Task Force of the Standing Committee for International Clinical Studies Including Therapeutic Trials (ESCISIT)," *Annals of the Rheumatic Diseases* **62**, 1145–1155 (2003).

[17] K. M. Jordan, S. Sawyer, P. Coakley, H. E. Smith, C. Cooper, and N. K. Arden, "The use of conventional and complementary treatments for knee osteoarthritis in the community," *Rheumatology* **43**, 381–384 (2004).

[18] R. Christensen, A. Astrup, and H. Bliddal, "Weight loss: the treatment of choice for knee osteoarthritis? A randomized trial," *Osteoarthritis and Cartilage* **13**, 20–27 (2005).

[19] S. P. Messier, R. F. Loeser, G. D. Miller, T. M. Morgan, W. J. Rejeski, M. A. Sevick, W. H. Ettinger, M. Pahor, and J. D. Williamson, "Exercise and dietary weight loss in overweight and obese older adults with knee osteoarthritis: the Arthritis, Diet, and Activity Promotion Trial," *Arthritis and Rheumatism* **50**, 1501–1510 (2004).

[20] F. W. Roemer, F. Eckstein, D. Hayashi, and A. Guermazi, "The role of imaging in osteoarthritis," *Best Practice and Research: Clinical Rheumatology* **28**, 31–60 (2014).

[21] N. H. Varady and A. J. Grodzinsky, "Osteoarthritis year in review 2015: Mechanics," *Osteoarthritis and Cartilage* **24**, 27–35 (2016).

[22] S. Demehri, N. Hafezi-Nejad, and J. A. Carrino, "Conventional and novel imaging modalities in osteoarthritis: current state of the evidence," *Current Opinion in Rheumatology* **27**, 295–303 (2015).

[23] J. Rautiainen, M. J. Nissi, E.-N. Salo, V. Tiitu, M. A. Finnilä, O.-M. Aho, S. Saarakkala, P. Lehenkari, J. Ellermann, and M. T. Nieminen, "Multiparametric MRI assessment of human articular cartilage degeneration: Correlation with quantitative histology and mechanical properties: Multiparametric Assessment of Cartilage Degeneration," *Magnetic Resonance in Medicine* **74**, 249–259 (2015).

[24] X. Li and S. Majumdar, "Quantitative MRI of articular cartilage and its clinical applications," *Journal of Magnetic Resonance Imaging* **38**, 991–1008 (2013).

[25] G. E. Gold, C. A. Chen, S. Koo, B. A. Hargreaves, and N. K. Bangerter, "Recent advances in MRI of articular cartilage," *American Journal of Roentgenology* **193**, 628–638 (2009).

[26] E. Kaleva, T. Virén, S. Saarakkala, J. Sahlman, J. Sirola, J. Puhakka, T. Paatela, H. Kroger, I. Kiviranta, J. S. Jurvelin, and J. Töyräs, "Arthroscopic Ultrasound Assessment of Articular Cartilage in the Human Knee Joint: A Potential Diagnostic Method," *Cartilage* **2**, 246–253 (2011).

[27] T. Virén, M. Timonen, H. Tyrvainen, V. Tiitu, J. S. Jurvelin, and J. Töyräs, "Ultrasonic evaluation of acute impact injury of articular cartilage in vitro," *Osteoarthritis and Cartilage* **20**, 719–726 (2012).

[28] T. Virén, S. Saarakkala, V. Tiitu, J. Puhakka, I. Kiviranta, J. Jurvelin, and J. Töyräs, "Ultrasound evaluation of mechanical injury of bovine knee articular cartilage under arthroscopic control," *IEEE Transactions on Ultrasonics, Ferroelectrics, and Frequency Control* **58**, 148–155 (2011).

[29] J. Liukkonen, J. Hirvasniemi, A. Joukainen, P. Penttilä, T. Virén, S. Saarakkala, H. Kröger, J. S. Jurvelin, and J. Töyräs, "Arthroscopic Ultrasound Technique for Simultaneous Quantitative Assessment of Articular Cartilage and Subchondral Bone: An In Vitro and In Vivo Feasibility Study," *Ultrasound in Medicine and Biology* **39**, 1460–1468 (2013).

[30] J. Podlipská, J. M. Koski, P. Pulkkinen, and S. Saarakkala, "In Vivo Quantitative Ultrasound Image Analysis of Femoral Subchondral Bone in Knee Osteoarthritis," *The Scientific World Journal* **2013**, 182562 (2013).

[31] J. Podlipská, A. Guermazi, P. Lehenkari, J. Niinimäki, F. W. Roemer, J. P. Arokoski, P. Kaukinen, E. Liukkonen, E. Lammentausta, M. T. Nieminen, O. Tervonen, J. M. Koski, and S. Saarakkala, "Comparison of Diagnostic Performance of Semi-Quantitative Knee Ultrasound and Knee Radiography with MRI: Oulu Knee Osteoarthritis Study," *Scientific Reports* **6**, 22365 (2016).

[32] J. M. Koski, A. Kamel, P. Waris, V. Waris, I. Tarkiainen, E. Karvanen, M. Szkudlarek, S. Z. Aydin, E. Alasaarela, W. Schmidt, E. De Miguel, P. Mandl, E. Filippucci, H. Ziswiler, L. Terslev, K. Áts, R. Kurucz, E. Naredo, P. Balint, A. Iagnocco, S. Lepojärvi, A. Elseoud, M. Fouda, and S. Saarakkala, "Atlas-based knee osteophyte assessment with ultrasonography and radiography: relationship to arthroscopic degeneration of articular cartilage," *Scandinavian Journal of Rheumatology* **45**, 158–164 (2016).

[33] S. Saarakkala, M. S. Laasanen, J. S. Jurvelin, and J. Töyräs, "Quantitative ultrasound imaging detects degenerative changes in articular cartilage surface and subchondral bone," *Physics in Medicine and Biology* **51**, 5333–5346 (2006).

[34] E. Chérin, A. Saïed, P. Laugier, P. Netter, and G. Berger, "Evaluation of acoustical parameter sensitivity to age-related and osteoarthritic changes in articular cartilage using 50-MHz ultrasound," *Ultrasound in Medicine and Biology* **24**, 341–354 (1998).

[35] E. Chérin, A. Saïed, B. Pellaumail, D. Loeuille, P. Laugier, P. Gillet, P. Netter, and G. Berger, "Assessment of rat articular cartilage maturation using 50-MHz quantitative ultrasonography," *Osteoarthritis and Cartilage* **9**, 178–186 (2001).

[36] A. S. Aula, J. Töyräs, V. Tiitu, and J. S. Jurvelin, "Simultaneous ultrasound measurement of articular cartilage and subchondral bone," *Osteoarthritis and Cartilage* **18**, 1570–1576 (2010).

[37] E. Naredo, C. Acebes, I. Möller, F. Canillas, J. J. de Agustin, E. de Miguel, E. Filippucci, A. Iagnocco, C. Moragues, R. Tuneu, J. Uson, J. Garrido, E. Delgado-Baeza, and I. Sáenz-Navarro, "Ultrasound validity in the measurement of knee cartilage thickness.," *Annals of the Rheumatic Diseases* **68**, 1322–1327 (2009).

[38] D. R. Eyre and H. Muir, "The distribution of different molecular species of collagen in fibrous, elastic and hyaline cartilages of the pig.," *The Biochemical Journal* **151**, 595–602 (1975).

[39] M. Benjamin and E. J. Evans, "Fibrocartilage," *Journal of Anatomy* **171**, 1–15 (1990).

[40] V. C. Mow, A. Ratcliffe, and A. R. Poole, "Cartilage and diarthrodial joints as paradigms for hierarchical materials and structures," *Biomaterials* **13**, 67–97 (1992).

[41] H. Forster and J. Fisher, "The influence of loading time and lubricant on the friction of articular cartilage," *Proceedings of the Institution of Mechanical Engineers, Part H: Journal of Engineering in Medicine* **210**, 109–119 (1996).

[42] C. G. Armstrong and V. C. Mow, "Variations in the intrinsic mechanical properties of human articular cartilage with age, degeneration, and water content," *The Journal of Bone and Joint Surgery* **64**, 88–94 (1982).

[43] E. B. Hunziker, T. M. Quinn, and H.-J. Häuselmann, "Quantitative structural organization of normal adult human articular cartilage," *Osteoarthritis and Cartilage* **10**, 564–572 (2002).

[44] D. Eyre, "Collagen of articular cartilage," *Arthritis Research* **4**, 30–35 (2002).

[45] K. Gelse, E. Pöschl, and T. Aigner, "Collagens - Structure, function, and biosynthesis," *Advanced Drug Delivery Reviews* **55**, 1531–1546 (2003).

[46] A. J. Sophia Fox, A. Bedi, and S. A. Rodeo, "The Basic Science of Articular Cartilage: Structure, Composition, and Function," *Sports Health: A Multidisciplinary Approach* **1**, 461–468 (2009).

[47] J. A. Buckwalter and H. J. Mankin, "Articular cartilage: tissue design and chondrocyte-matrix interactions," *Instructional Course Lectures* **47**, 477–486 (1998).

[48] D. R. Eyre and J. J. Wu, "Collagen structure and cartilage matrix integrity," *The Journal of Rheumatology. Supplement* **43**, 82–85 (1995).

[49] N. D. Broom, "Further insights into the structural principles governing the function of articular cartilage," *Journal of Anatomy* **139 (Pt 2**, 275–294 (1984).

[50] A. K. Williamson, A. C. Chen, K. Masuda, E. J.-M. A. Thonar, and R. L. Sah, "Tensile mechanical properties of bovine articular cartilage: variations with growth and relationships to collagen network components," *Journal of Orthopaedic Research* **21**, 872–880 (2003).

[51] H. Muir, P. Bullough, and A. Maroudas, "The distribution of collagen in human articular cartilage with some of its physiological implications," *Journal of Bone and Joint Surgery* **52**, 554–563 (1970).

[52] J. P. Arokoski, M. M. Hyttinen, T. Lapvetelainen, P. Takács, B. Kosztáczky, L. Módis, V. Kovanen, and H. Helminen, "Decreased birefringence of the superficial zone collagen network in the canine knee (stifle) articular cartilage after long distance running training, detected by quantitative polarised light microscopy," *Annals of the Rheumatic Diseases* **55**, 253–264 (1996).

[53] W. S. Hwang, B. Li, L. H. Jin, K. Ngo, N. S. Schachar, and G. N. Hughes, "Collagen fibril structure of normal, aging, and osteoarthritic cartilage," *The Journal of Pathology* **167**, 425–433 (1992).

[54] R. J. Minns and F. S. Steven, "The collagen fibril organization in human articular cartilage," *Journal of Anatomy* **123**, 437–457 (1977).

[55] P. J. Roughley, "The structure and function of cartilage proteoglycans," *European Cells & Materials* **12**, 92–101 (2006).

[56] H. Muir, "Proteoglycans as organizers of the intercellular matrix," *Biochemical Society Transactions* **11**, 613–622 (1983).

[57] A. Maroudas, "Physicochemical Properties of Cartilage in the Light of Ion Exchange Theory," *Biophysical Journal* **8**, 575–595 (1968).

[58] G. E. Kempson, H. Muir, S. A. Swanson, and M. A. Freeman, "Correlations between stiffness and the chemical constituents of cartilage on the human femoral head," *Biochimica et Biophysica Acta* **215**, 70–77 (1970).

[59] H. Muir, "The chondrocyte, architect of cartilage. Biomechanics, structure, function and molecular biology of cartilage matrix macromolecules," *BioEssays* **17**, 1039–1048 (1995).

[60] B. Rolauffs, J. M. Williams, A. J. Grodzinsky, K. E. Kuettner, and A. A. Cole, "Distinct horizontal patterns in the spatial organization of superficial zone chondrocytes of human joints," *Journal of Structural Biology* **162**, 335–344 (2008).

[61] K. D. Jadin, B. L. Wong, W. C. Bae, K. W. Li, A. K. Williamson, B. L. Schumacher, J. H. Price, and R. L. Sah, "Depth-varying density and organization of chondrocytes in immature and mature bovine articular cartilage assessed by 3d imaging and analysis.," *The Journal of Histochemistry & Cytochemistry* **53**, 1109–19 (2005).

[62] C. A. Poole, "Articular cartilage chondrons: form, function and failure," *Journal of Anatomy* **191 (Pt 1)**, 1–13 (1997).

[63] S. Söder, L. Hambach, R. Lissner, T. Kirchner, and T. Aigner, "Ultrastructural localization of type VI collagen in normal adult and osteoarthritic human articular cartilage," *Osteoarthritis and Cartilage* **10**, 464–470 (2002).

[64] M. L. Gray, A. M. Pizzanelli, A. J. Grodzinsky, and R. C. Lee, "Mechanical and physiochemical determinants of the chondrocyte biosynthetic response," *Journal of Orthopaedic Research* **6**, 777–792 (1988).

[65] P. Tanska, S. M. Turunen, S. K. Han, P. Julkunen, W. Herzog, and R. K. Korhonen, "Superficial Collagen Fibril Modulus and Pericellular Fixed Charge Density Modulate Chondrocyte Volumetric Behaviour in Early Osteoarthritis," *Computational and Mathematical Methods in Medicine* **2013**, 164146 (2013).

[66] J. A. Buckwalter, H. J. Mankin, and A. J. Grodzinsky, "Articular cartilage and osteoarthritis," *Instructional Course Lectures* **54**, 465–480 (2005).

[67] J. A. Buckwalter and H. J. Mankin, "Articular cartilage. Part II: Degeneration and Osteoarthrosis, Repair, Regeneration, and Transplantation," *The Journal of Bone & Joint Surgery* **79**, 612–632 (1997).

[68] J. A. Martin and J. A. Buckwalter, "Aging, articular cartilage chondrocyte senescence and osteoarthritis," *Biogerontology* **3**, 257–264 (2002).

[69] J. A. Gustafson, M. E. Robinson, G. K. Fitzgerald, S. Tashman, and S. Farrokhi, "Knee motion variability in patients with knee osteoarthritis: The effect of self-reported instability," *Clinical Biomechanics* **30**, 475–480 (2015).

[70] J. T. A. Mäkelä, S.-K. Han, W. Herzog, and R. K. Korhonen, "Very early osteoarthritis changes sensitively fluid flow properties of articular cartilage," *Journal of Biomechanics* **48**, 3369–3376 (2015).

[71] W. K. Aicher and B. Rolauffs, "The spatial organisation of joint surface chondrocytes: review of its potential roles in tissue functioning, disease and early, preclinical diagnosis of osteoarthritis," *Annals of the Rheumatic Diseases* **73**, 645–653 (2014).

[72] M. E. Adams and K. D. Brandt, "Hypertrophic repair of canine articular cartilage in osteoarthritis after anterior cruciate ligament transection," *The Journal of Rheumatology* **18**, 428–435 (1991).

[73] M. B. Goldring and M. Otero, "Inflammation in osteoarthritis," *Current Opinion in Rheumatology* **23**, 471–478 (2011).

[74] C. M. Balmaceda, "Evolving guidelines in the use of topical nonsteroidal anti-inflammatory drugs in the treatment of osteoarthritis.," *BMC Musculoskeletal Disorders* **15**, 27 (2014).

[75] H. Bliddal, A. R. Leeds, and R. Christensen, "Osteoarthritis, obesity and weight loss: evidence, hypotheses and horizons - a scoping review," *Obesity Reviews* **15**, 578–586 (2014).

[76] J. R. Steadman, W. G. Rodkey, S. B. Singleton, and K. K. Briggs, "Microfracture technique for full-thickness chondral defects: Technique and clinical results," *Operative Techniques in Orthopaedics* **7**, 300–304 (1997).

[77] R. J. Beaver, M. Mahomed, D. Backstein, A. Davis, D. J. Zukor, and A. E. Gross, "Fresh osteochondral allografts for post-traumatic defects in the knee. A survivorship analysis," *The Journal of Bone and Joint Surgery* **74**, 105–110 (1992).

[78] M. Brittberg, A. Lindahl, A. Nilsson, C. Ohlsson, O. Isaksson, and L. Peterson, "Treatment of Deep Cartilage Defects in the Knee with Autologous Chondrocyte Transplantation.," *The New England Journal of Medicine* **331**, 889–895 (1994).

[79] P. Lobenhoffer and J. D. Agneskirchner, "Improvements in surgical technique of valgus high tibial osteotomy," *Knee surgery, Sports Traumatology, Arthroscopy* **11**, 132–138 (2003).

[80] C. Y. J. Wenham, A. J. Grainger, and P. G. Conaghan, "The role of imaging modalities in the diagnosis, differential diagnosis and clinical assessment of peripheral joint osteoarthritis," *Osteoarthritis and Cartilage* **22**, 1692–1702 (2014).

[81] M. Brittberg and C. S. Winalski, "Evaluation of cartilage injuries and repair," *The Journal of Bone and Joint Surgery. American Volume* **85-A Suppl**, 58–69 (2003).

[82] B. H. Brismar, T. Wredmark, T. Movin, J. Leandersson, and O. Svensson, "Observer reliability in the arthroscopic classification of osteoarthritis of the knee," *The Journal of Bone and Joint Surgery (Br)* **84-B**, 42–47 (2002).

[83] G. Spahn, H. M. Klinger, M. Baums, U. Pinkepank, and G. O. Hofmann, "Reliability in arthroscopic grading of cartilage lesions: results of a prospective blinded study for evaluation of inter-observer reliability," *Archives of Orthopaedic and Trauma Surgery* **131**, 377–381 (2011).

[84] N. C. R. te Moller, H. Brommer, J. Liukkonen, T. Virén, M. Timonen, P. H. Puhakka, J. S. Jurvelin, P. R. van Weeren, and J. Töyräs, "Arthroscopic Optical Coherence Tomography Provides Detailed Information on Articular Cartilage Lesions in Horses," *Veterinary Journal* **197**, 589–595 (2013).

[85] T. Niemelä, T. Virén, J. Liukkonen, D. Argüelles, N. C. R. te Moller, P. H. Puhakka, J. S. Jurvelin, R.-M. Tulamo, and J. Töyräs, "Application of optical coherence tomography enhances reproducibility of arthroscopic evaluation of equine joints," *Acta Veterinaria Scandinavica* **56**, 3 (2014).

[86] P. H. Puhakka, N. C. R. Te Moller, I. O. Afara, J. T. A. Mäkelä, V. Tiitu, R. K. Korhonen, H. Brommer, T. Virén, J. S. Jurvelin, and J. Töyräs, "Estimation of articular cartilage properties using multivariate analysis of optical coherence tomography signal," *Osteoarthritis and Cartilage* **23**, 2206–2213 (2015).

[87] N. Männicke, M. Schöne, M. Gottwald, F. Göbel, M. L. Oelze, and K. Raum, "3-D High-Frequency Ultrasound Backscatter Analysis of Human Articular Cartilage," *Ultrasound in Medicine and Biology* **40**, 244–257 (2014).

[88] P. Penttilä, J. Liukkonen, A. Joukainen, T. Virén, J. S. Jurvelin, J. Töyräs, and H. Kröger, "Diagnosis of Knee Osteochondral Lesions With Ultrasound Imaging," *Arthroscopy Techniques* **4**, e429–e433 (2015).

[89] P. N. T. Wells, *Biomedical Ultrasonics* (Academic Press, London ; New York, 1977).

[90] B. A. Auld, *Acoustic fields and waves in solids, Vol 1*, 2nd ed ed. (R.E. Krieger Publishing Company, 1990).

[91] J. L. Rose, *Ultrasonic waves in solid media* (Cambridge Univ. Press, Cambridge, 2004).

[92] K. K. Shung, *Ultrasonic Scattering in Biological Tissues*, Vol. 94, 1993).

[93] L. E. Kinsler, ed., *Fundamentals of acoustics*, 4th ed ed. (Wiley, New York, 2000).

[94] J. J. Faran, "Sound Scattering by Solid Cylinders and Spheres," *The Journal of the Acoustical Society of America* **23**, 405–418 (1951).

[95] J. Mamou and M. L. Oelze, eds., *Quantitative ultrasound in soft tissues* (Springer, Dordrecht, 2013).

[96] L. X. Yao, J. A. Zagzebski, and E. L. Madsen, "Backscatter Coefficient Measurements Using a Reference Phantom to Extract Depth-Dependent Instrumentation Factors," *Ultrasonic Imaging* **12**, 58–70 (1990).

[97] A. B. Bhatia, *Ultrasonic absorption: an introduction to the theory of sound absorption and dispersion in gases, liquids, and solids* (Dover Publications, New York, 1985).

[98] F. S. Foster, K. a. Harasiewicz, and M. D. Sherar, "A history of medical and biological imaging with polyvinylidene fluoride (PVDF) transducers.," *IEEE Transactions on Ultrasonics, Ferroelectrics, and Frequency Control* **47**, 1363–1371 (2000).

[99] I. Möller, D. Bong, E. Naredo, E. Filippucci, I. Carrasco, C. Moragues, and A. Iagnocco, "Ultrasound in the study and monitoring of osteoarthritis.," *Osteoarthritis and Cartilage* **16 Suppl 3**, S4–S7 (2008).

[100] S. Saarakkala, "Diagnostic performance of knee ultrasonography for detecting degenerative changes of articular cartilage," *Osteoarthritis and Cartilage* **20**, 376–381 (2012).

[101] A. Iagnocco, E. Filippucci, A. Ossandon, A. Ciapetti, F. Salaffi, S. Basili, W. Grassi, and G. Valesini, "High resolution ultrasonography in detection of bone erosions in patients with hand osteoarthritis," *Journal of Rheumatology* **32**, 2381–2383 (2005).

[102] H. I. Keen, F. Lavie, R. J. Wakefield, M.-A. D'Agostino, H. B. Hammer, E. Hensor, A. Pendleton, D. Kane, H. Guerini, C. Schueller-Weidekamm, M. C. Kortekaas, F. Birrel, M. Kloppenburg, T. Stamm, I. Watt, J. S. Smolen, E. Maheu, M. Dougados, and P. G. Conaghan, "The development of a preliminary ultrasonographic scoring system for features of hand osteoarthritis.," *Annals of the Rheumatic Diseases* **67**, 651–655 (2008).

[103] A. Iagnocco, C. Perricone, C. Scirocco, F. Ceccarelli, M. Modesti, A. Gattamelata, C. Vavala, I. M. Rutigliano, A. Musetescu, and G. Valesini, "The interobserver reliability of ultrasound in knee osteoarthritis," *Rheumatology* **51**, 2013–2019 (2012).

[104] K. Hattori, Y. Takakura, M. Ishimura, T. Habata, K. Uematsu, and K. Ikeuch, "Quantitative arthroscopic ultrasound evaluation of living human cartilage," *Clinical Biomechanics* **19**, 213–216 (2004).

[105] K. Hattori, Y. Takakura, Y. Tanaka, T. Habata, T. Kumai, K. Uematsu, K. Sugimoto, and K. Ikeuchi, "Quantitative ultrasound can assess living human cartilage," *The Journal of Bone and Joint Surgery* **88 Suppl 4**, 201–212 (2006).

[106] Y.-P. Huang and Y.-P. Zheng, "Intravascular Ultrasound (IVUS): A Potential Arthroscopic Tool for Quantitative Assessment of Articular Cartilage," *The Open Biomedical Engineering Journal* **3**, 13–20 (2009).

[107] T. Virén, S. Saarakkala, E. Kaleva, H. J. Nieminen, J. S. Jurvelin, and J. Töyräs, "Minimally Invasive Ultrasound Method for Intra-Articular Diagnostics of Cartilage Degeneration," *Ultrasound in Medicine & Biology* **35**, 1546–1554 (2009).

[108] J. Puhakka, I. O. Afara, T. Paatela, M. J. Sormaala, M. A. Timonen, T. Virén, J. S. Jurvelin, J. Töyräs, and I. Kiviranta, "In Vivo Evaluation of the Potential of High-Frequency Ultrasound for Arthroscopic Examination of the Shoulder Joint," *Cartilage* **7**, 248–255 (2016).

[109] J. Liukkonen, P. Lehenkari, J. Hirvasniemi, A. Joukainen, T. Virén, S. Saarakkala, M. T. Nieminen, J. S. Jurvelin, and J. Töyräs, "Ultrasound Arthroscopy of Human Knee Cartilage and Subchondral Bone In Vivo," *Ultrasound in Medicine & Biology* **40**, 2039–2047 (2014).

[110] E. Kaleva, S. Saarakkala, J. S. Jurvelin, T. Virén, and J. Töyräs, "Effects of Ultrasound Beam Angle and Surface Roughness on the Quantitative Ultrasound Parameters of Articular Cartilage," *Ultrasound in Medicine & Biology* **35**, 1344–1351 (2009).

[111] R. A. Lemons and Quate C. F., "Acoustic microscope—scanning version," *Applied Physics Letters* **24**, 163–165 (1974).

[112] S. Leicht and K. Raum, "Acoustic impedance changes in cartilage and subchondral bone due to primary arthrosis," *Ultrasonics* **48**, 613–620 (2008).

[113] Y. Sun, D. Responte, H. Xie, J. Liu, H. Fatakdawala, J. Hu, K. A. Athanasiou, and L. Marcu, "Nondestructive Evaluation of Tissue Engineered Articular Cartilage Using Time-Resolved Fluorescence Spectroscopy and Ultrasound Backscatter Microscopy," *Tissue Engineering Part C: Methods* **18**, 215–226 (2012).

[114] M. Schöne, N. Männicke, M. Gottwald, F. Göbel, and K. Raum, "3-D High-Frequency Ultrasound Improves the Estimation of Surface Properties in Degenerated Cartilage," *Ultrasound in Medicine & Biology* **39**, 834–844 (2013).

[115] M. Schöne, N. Männicke, J. S. Somerson, B. Marquaß, R. Henkelmann, J. Mochida, T. Aigner, K. Raum, and R. M. Schulz, "3D ultrasound biomicroscopy for assessment of cartilage repair tissue: volumetric characterisation and correlation to established classification systems," *European Cells & Materials* **31**, 119–135 (2016).

[116] E. Kaleva, J. Töyräs, J. S. Jurvelin, T. Virén, and S. Saarakkala, "Effects of ultrasound frequency, temporal sampling frequency, and spatial sampling step on the quantitative ultrasound parameters of articular cartilage," *IEEE Transactions on Ultrasonics, Ferroelectrics, and Frequency Control* **56**, 1383–1393 (2009).

[117] A. Saïed, E. Chérin, H. Gaucher, P. Laugier, P. Gillet, J. Floquet, P. Netter, and G. Berger, "Assessment of articular cartilage and subchondral bone: subtle and progressive changes in experimental osteoarthritis using 50 MHz echography in vitro," *Journal of Bone Mineral and Research* **12**, 1378–1386 (1997).

[118] X. Zhao, S. Wilkinson, R. Akhtar, M. J. Sherratt, R. E. B. Watson, and B. Derby, "Quantifying Micro-mechanical Properties of Soft Biological Tissues with Scanning Acoustic Microscopy," *Materials Research Society Symposium Proceedings* **1301** (2011).

[119] R. S. Adler, D. K. Dedrick, T. J. Laing, E. H. Chiang, C. R. Meyer, P. H. Bland, and J. M. Rubin, "Quantitative assessment of cartilage surface roughness in osteoarthritis using high frequency ultrasound," *Ultrasound in Medicine & Biology* **18**, 51–58 (1992).

[120] S. Z. Wang, Y. P. Huang, S. Saarakkala, and Y. P. Zheng, "Quantitative assessment of articular cartilage with morphologic, acoustic and mechanical properties obtained using high-frequency ultrasound," *Ultrasound in Medicine & Biology* **36**, 512–527 (2010).

[121] H. J. Nieminen, Y. Zheng, S. Saarakkala, Q. Wang, J. Töyräs, Y. Huang, and J. Jurvelin, "Quantitative assessment of articular cartilage using high-frequency ultrasound: research findings and diagnostic prospects," *Critical Reviews in Biomedical Engineering* **37**, 461–494 (2009).

[122] S. Saarakkala, J. Töyräs, J. Hirvonen, M. S. Laasanen, R. Lappalainen, and J. S. Jurvelin, "Ultrasonic quantitation of superficial degradation of articular cartilage," *Ultrasound in Medicine & Biology* **30**, 783–792 (2004).

[123] M. S. Laasanen, S. Saarakkala, J. Töyräs, J. Rieppo, and J. S. Jurvelin, "Site-specific ultrasound reflection properties and superficial collagen content of bovine knee articular cartilage," *Physics in Medicine and Biology* **50**, 3221–3233 (2005).

[124] M. S. Laasanen, J. Töyräs, A. Vasara, S. Saarakkala, M. M. Hyttinen, I. Kiviranta, and J. S. Jurvelin, "Quantitative ultrasound imaging of spontaneous repair of porcine cartilage," *Osteoarthritis and Cartilage* **14**, 258–263 (2006).

[125] T. Virén, S. Saarakkala, J. S. Jurvelin, H. Pulkkinen, V. Tiitu, P. Valonen, I. Kiviranta, M. J. Lammi, and J. Töyräs, "Quantitative Evaluation of Spontaneously and Surgically Repaired Rabbit Articular Cartilage Using Intra-Articular Ultrasound Methodin situ," *Ultrasound in Medicine & Biology* **36**, 833–839 (2010).

[126] K. Gelse, A. Olk, S. Eichhorn, B. Swoboda, M. Schoene, and K. Raum, "Quantitative ultrasound biomicroscopy for the analysis of healthy and repair cartilage tissue," *European Cells & Materials* **19**, 58–71 (2010).

[127] J. Töyräs, J. Rieppo, M. T. Nieminen, H. J. Helminen, and J. S. Jurvelin, "Characterization of Enzymatically Induced Degradation of Articular Cartilage Using High Frequency Ultrasound," *Physics in Medicine and Biology* **44**, 2723–2733 (1999).

[128] D. H. Agemura, W. D. O'Brien Jr, J. E. Olerud, L. E. Chun, and D. E. Eyre, "Ultrasonic propagation properties of articular cartilage at 100 MHz," *The Journal of the Acoustical Society of America* **87**, 1786–1791 (1990).

[129] S. G. Patil and Y. P. Zheng, "Measurement of ultrasound speed of articular cartilage in variable conditions," *Conference Proceedings IEEE Engineering in Medicine and Biology Society* **2**, 1341–1344 (2004).

[130] S. G. Patil, Y. P. Zheng, J. Y. Wu, and J. Shi, "Measurement of depth-dependence and anisotropy of ultrasound speed of bovine articular cartilage in vitro," *Ultrasound in Medicine & Biology* **30**, 953–963 (2004).

[131] P. H. Puhakka, N. C. R. te Moller, P. Tanska, S. Saarakkala, V. Tiitu, R. K. Korhonen, H. Brommer, T. Virén, J. S. Jurvelin, and J. Töyräs, "Optical coherence tomography enables accurate measurement of equine cartilage thickness for determination of speed of sound," *Acta Orthopaedica* **87**, 418–424 (2016).

[132] D. A. Senzig, F. K. Forster, and J. E. Olerud, "Ultrasonic attenuation in articular cartilage," *The Journal of the Acoustical Society of America* **92**, 676–681 (1992).

[133] H. J. Nieminen, S. Saarakkala, M. S. Laasanen, J. Hirvonen, J. S. Jurvelin, and J. Töyräs, "Ultrasound attenuation in normal and spontaneously degenerated articular cartilage," *Ultrasound in Medicine and Biology* **30**, 493–500 (2004).

[134] K. Hattori, K. Mori, T. Habata, Y. Takakura, and K. Ikeuchi, "Measurement of the mechanical condition of articular cartilage with an ultrasonic probe: quantitative evaluation using wavelet transformation," *Clinical Biomechanics* **18**, 553–557 (2003).

[135] E. Kaleva, S. Saarakkala, J. Töyräs, H. J. Nieminen, and J. S. Jurvelin, "In-vitro comparison of time-domain, frequency-domain and wavelet ultrasound parameters in diagnostics of cartilage degeneration," *Ultrasound in Medicine & Biology* **34**, 155–159 (2008).

[136] H. J. Nieminen, J. Töyräs, M. S. Laasanen, and J. S. Jurvelin, "Acoustic properties of articular cartilage under mechanical stress," *Biorheology* **43**, 523–535 (2006).

[137] J. Q. Yao and B. B. Seedhom, "Ultrasonic measurement of the thickness of human articular cartilage in situ," *Rheumatology* **38**, 1269–1271 (1999).

[138] R. W. Mann, "Comment on 'ultrasonic measurement of the thickness of human articular cartilage in situ' by Yao and Seedhom," *Rheumatology (Oxford, England)* **40**, 829–831 (2001).

[139] N. Männicke, M. Schöne, J. Liukkonen, D. Fachet, S. Inkinen, M. K. Malo, M. L. Oelze, J. Töyräs, J. S. Jurvelin, and K. Raum, "Species-Independent Modeling of High-Frequency Ultrasound Backscatter in Hyaline Cartilage," *Ultrasound in Medicine & Biology* **42**, 1375–1384 (2016).

[140] G. A. Joiner, E. R. Bogoch, K. P. Pritzker, M. D. Buschmann, A. Chevrier, and F. S. Foster, "High frequency acoustic parameters of human and bovine articular cartilage following experimentally-induced matrix degradation," *Ultrasonic Imaging* **23**, 106–116 (2001).

[141] E. Bossy, M. Talmant, and P. Laugier, "Effect of bone cortical thickness on velocity measurements using ultrasonic axial transmission: a 2D simulation study," *The Journal of the Acoustical Society of America* **112**, 297–307 (2002).

[142] E. Bossy, M. Talmant, and P. Laugier, "Three-dimensional simulations of ultrasonic axial transmission velocity measurement on cortical bone models," *The Journal of the Acoustical Society of America* **115**, 2314–2324 (2004).

[143] A. Hosokawa, "Ultrasonic pulse waves in cancellous bone analyzed by finite-difference time-domain methods," *Ultrasonics* **44 Suppl 1**, e227–231 (2006).

[144] J. J. Kaufman, G. Luo, and R. S. Siffert, "Ultrasound simulation in bone," *IEEE Transactions on Ultrasonics, Ferroelectrics, and Frequency cControl* **55**, 1205–1218 (2008).

[145] B. E. Treeby and B. T. Cox, "k-Wave: MATLAB toolbox for the simulation and reconstruction of photoacoustic wave fields," *Journal of Biomedical Optics* **15**, 021314 (2010).

[146] D. Cassereau, P. Nauleau, A. Bendjoudi, J. G. Minonzio, P. Laugier, E. Bossy, and Q. Grimal, "A hybrid FDTD-Rayleigh integral computational method for the simulation of the ultrasound measurement of proximal femur," *Ultrasonics* **54**, 1197–1202 (2014).

[147] Q. Grimal, D. Rohrbach, J. Grondin, R. Barkmann, C. C. Glüer, K. Raum, and P. Laugier, "Modeling of femoral neck cortical bone for the numerical simulation of ultrasound propagation," *Ultrasound in Medicine and Biology* **40**, 1015–1026 (2014).

[148] B. Vafaeian, M. El-Rich, T. El-Bialy, and S. Adeeb, "The finite element method for micro-scale modeling of ultrasound propagation in cancellous bone," *Ultrasonics* **54**, 1663–1676 (2014).

[149] P. Laugier and G. Haïat, *Bone Quantitative Ultrasound* (Springer Netherlands, Dordrecht; New York, 2011).

[150] K. Firouzi, B. T. Cox, B. E. Treeby, and N. Saffari, "A first-order k-space model for elastic wave propagation in heterogeneous media," *The Journal of the Acoustical Society of America* **132**, 1271–1283 (2012).

[151] Y. Kane, "Numerical solution of initial boundary value problems involving maxwell's equations in isotropic media," *IEEE Transactions on Antennas and Propagation* **14**, 302–307 (1966).

[152] J. Virieux, "P-SV wave propagation in heterogeneous media: Velocity-stress finite-difference method," *Geophysics* **51**, 889–901 (1986).

[153] F. Collino and C. Tsogka, "Application of the perfectly matched absorbing layer model to the linear elastodynamic problem in anisotropic heterogeneous media," *Geophysics* **66**, 294–307 (2001).

[154] C. T. M. Eneh, J. Liukkonen, M. K. H. Malo, J. S. Jurvelin, and J. Töyräs, "Inter-individual changes in cortical bone three-dimensional microstructure and elastic coefficient have opposite effects on radial sound speed," *The Journal of the Acoustical Society of America* **138**, 3491–3499 (2015).

[155] P. J. Basser, R. Schneiderman, R. A. Bank, E. Wachtel, and A. Maroudas, "Mechanical properties of the collagen network in human articular cartilage as measured by osmotic stress technique," *Archives of Biochemistry and Biophysics* **351**, 207–219 (1998).

[156] M. K. H. Malo, D. Rohrbach, H. Isaksson, J. Töyräs, J. S. Jurvelin, I. S. Tamminen, H. Kröger, and K. Raum, "Longitudinal elastic properties and porosity of cortical bone tissue vary with age in human proximal femur," *Bone* **53**, 451–458 (2013).

[157] D. Rohrbach, H. O. Lloyd, R. H. Silverman, and J. Mamou, "Fine-resolution maps of acoustic properties at 250 MHz of unstained fixed murine retinal layers," *The Journal of the Acoustical Society of America* **137**, EL381–7 (2015).

[158] Graves Robert W, "Simulating seismic wave propagation in 3D elastic media using staggered-grid finite differences," *Bulletin of the Seismological Society of America* **86**, 1091–1106 (1996).

[159] H. Fischer, I. Polikarpov, and A. F. Craievich, "Average protein density is a molecular-weight-dependent function," *Protein Science* **13**, 2825–2828 (2004).

[160] N. Hozumi, R. Yamashita, C. K. Lee, M. Nagao, K. Kobayashi, Y. Saijo, M. Tanaka, N. Tanaka, and S. Ohtsuki, "Time-frequency analysis for pulse driven ultrasonic microscopy for biological tissue characterization," *Ultrasonics* **42**, 717–722 (2004).

[161] D. Rohrbach, A. Jakob, H. Lloyd, S. Tretbar, R. H. Silverman, and J. Mamou, "A Novel Quantitative 500-MHz Acoustic-microscopy System for Ophthalmologic Tissues," *IEEE Transactions on Biomedical Engineering* (2016).

[162] J. W. Tukey, *Exploratory Data Analysis* (Addison-Wesley Pub. Co, Reading, Mass, 1977).

[163] N. P. Camacho, P. West, P. A. Torzilli, and R. Mendelsohn, "FTIR microscopic imaging of collagen and proteoglycan in bovine cartilage," *Biopolymers* **62**, 1–8 (2001).

[164] J. Rieppo, J. Hallikainen, J. S. Jurvelin, I. Kiviranta, H. J. Helminen, and M. M. Hyttinen, "Practical considerations in the use of polarized light microscopy in the analysis of the collagen network in articular cartilage," *Microscopy Research and Technique* **71**, 279–287 (2008).

[165] K. Király, T. Lapveteläinen, J. Arokoski, K. Törrönen, L. Módis, I. Kiviranta, and H. J. Helminen, "Application of selected cationic dyes for the semiquantitative estimation of glycosaminoglycans in histological sections of articular cartilage by microspectrophotometry," *The Histochemical journal* **28**, 577–590 (1996).

[166] M. C. Kolios, G. J. Czarnota, M. Lee, J. W. Hunt, and M. D. Sherar, "Ultrasonic spectral parameter characterization of apoptosis," *Ultrasound in Medicine & Biology* **28**, 589–597 (2002).

[167] R. K. Saha and M. C. Kolios, "Effects of cell spatial organization and size distribution on ultrasound backscattering," *IEEE Transactions on Ultrasonics, Ferroelectrics, and Frequency Control* **58**, 2118–2131 (2011).

[168] A. Han, R. Abuhabsah, R. J. Miller, S. Sarwate, and W. D. O'Brien, "The measurement of ultrasound backscattering from cell pellet biophantoms and tumors ex vivo," *The Journal of the Acoustical Society of America* **134**, 686–693 (2013).

[169] I. Youn, J. B. Choi, L. Cao, L. A. Setton, and F. Guilak, "Zonal variations in the three-dimensional morphology of the chondron measured in situ using confocal microscopy," *Osteoarthritis and Cartilage* **14**, 889–897 (2006).

[170] H. J. Mankin and L. Lippiello, "Biochemical and metabolic abnormalities in articular cartilage from osteo-arthritic human hips," *The Journal of Bone and Joint Surgery* **52**, 424–434 (1970).

[171] Y. Hoshiyama, S. Otsuki, S. Oda, Y. Kurokawa, M. Nakajima, T. Jotoku, R. Tamura, Y. Okamoto, M. K. Lotz, and M. Neo, "Chondrocyte Clusters Adjacent to Sites of Cartilage Degeneration Have Characteristics of Progenitor Cells," *Journal of Orthopaedic Research* **33**, 548–555 (2015).

[172] N. Männicke, M. Schöne, M. Oelze, and K. Raum, "Articular cartilage degeneration classification by means of high-frequency ultrasound," *Osteoarthritis and Cartilage* **22**, 1577–1582 (2014).

[173] K. A. Wear, R. F. Wagner, M. F. Insana, and T. J. Hall, "Application of autoregressive spectral analysis to cepstral estimation of mean scatterer spacing," *IEEE Transactions on Ultrasonics, Ferroelectrics, and Frequency Control* **40**, 50–58 (1993).

[174] R. J. Minns, F. S. Steven, and K. Hardinge, "Osteoarthrotic articular cartilage lesions of the femoral head observed in the scanning electron microscope," *The Journal of Pathology* **122**, 63–70 (1977).

[175] B. K. Hoffmeister, A. K. Wong, E. D. Verdonk, S. A. Wickline, and J. G. Miller, "Comparison of the anisotropy of apparent integrated ultrasonic backscatter from fixed human tendon and fixed human myocardium.," *The Journal of the Acoustical Society of America* **97**, 1307–1313 (1995).

[176] T. Virén, Y. P. Huang, S. Saarakkala, H. Pulkkinen, V. Tiitu, A. Linjama, I. Kiviranta, M. J. Lammi, A. Brünott, H. Brommer, R. Van Weeren, P. A. J. Brama, Y. P. Zheng, J. S. Jurvelin, and J. Töyräs, "Comparison of ultrasound and optical coherence tomography techniques for evaluation of integrity of spontaneously repaired horse cartilage," *Journal of Medical Engineering & Technology* **36**, 185–192 (2012).

[177] J. Rieppo, J. Töyräs, M. T. Nieminen, V. Kovanen, M. M. Hyttinen, R. K. Korhonen, J. S. Jurvelin, and H. J. Helminen, "Structure-function relationships in enzymatically modified articular cartilage," *Cells, Tissues, Organs* **175**, 121–132 (2003).

[178] E. B. Hunziker, K. Lippuner, and N. Shintani, "How best to preserve and reveal the structural intricacies of cartilaginous tissue," *Matrix Biology* **39**, 33–43 (2014).

[179] S. L. Myers, K. Dines, D. A. Brandt, K. D. Brandt, and M. E. Albrecht, "Experimental assessment by high frequency ultrasound of articular cartilage thickness and osteoarthritic changes," *The Journal of Rheumatology* **22**, 109–116 (1995).

[180] S. Tepic, T. Macirowski, and R. W. Mann, "Mechanical properties of articular cartilage elucidated by osmotic loading and ultrasound," *Proceedings of the National Academy of Sciences of the United States of America* **80**, 3331–3333 (1983).

SATU INKINEN

Arthroscopic ultrasound imaging has been proposed for diagnostics of cartilage degeneration and injuries. In this thesis, the effects of collagen and chondrocytes on ultrasound backscattering in articular cartilage were investigated experimentally and with simulations. Ultrasound backscatter was found to be sensitive to changes in the composition and structure of the collagen network and the distribution and density of chondrocytes. This encourages the use of quantitative ultrasound for clinical assessment of articular cartilage.

UNIVERSITY OF
EASTERN FINLAND

BIOPHYSICS
BONE AND CARTILAGE

uef.fi

PUBLICATIONS OF
THE UNIVERSITY OF EASTERN FINLAND
Dissertations in Forestry and Natural Sciences

ISBN 978-952-61-2467-4
ISSN 1798-5668